

# Tuberculosis Detection: A Comprehensive Review of State-of-the-Art Models

Mustapha Oloko-Oba and Serestina Viriri

**Abstract**—According to the World Health Organization, tuberculosis is one of the global sources of death. Tuberculosis is certainly curable, but it needs to be detected early. While several screening techniques exist, Chest X-Ray has been recommended by the World Health Organization as an essential diagnostic aid. Therefore, the automatic detection of tuberculosis from Chest X-Ray has become a crucial research focus in the Machine Learning and Deep Learning domain. This paper presents various traditional tuberculosis diagnosis tests with more emphasis on state-of-the-art models. The article discusses popular Machine Learning and Deep Learning architectures that have performed excellently on medical imaging to detect Chest X-Ray abnormalities; it summarizes prominent datasets and briefly discusses the steps used in detection models ranging from image pre-processing to feature extractions and features classifications. It also highlights the standard evaluation metrics used to measure different models' performance accuracy, strengths, and weaknesses. Lastly, it suggests some aspects that may bring about additional improvement in medical imaging analysis for tuberculosis diagnosis in the future.

**Index Terms**—Tuberculosis, Chest X-Ray, Machine Learning, Deep Learning, Computer-Aided Diagnostic, Pre-processing

## I. INTRODUCTION

ONE of the global sources of death as reported by the World Health Organization (WHO) is tuberculosis (TB) which mostly attacks the lungs but sometimes attacks other body parts [1]. TB infection is contagious and can be transmitted through the air by sneezing, spitting and coughing from an infected individual [2]. The majority of the infected individuals usually have TB in a latent state, which gradually advances into active TB if left undetected and untreated [3]. Typical indications of TB include persistent coughing, weight loss, fatigue, night sweats, and low fever [4], [5], [6]. Both men and women are at risk of contracting TB, although it is more prominent in men. As of 2018, about 1.2 million deaths were recorded from the 10 million estimated TB infected individuals, which is a decrease from the previous 1.3 million and 1.7 million deaths which were recorded in 2016 and 2011 respectively [1], [7]. The burden of TB is far more prevalent in developing regions [8] where high death tolls resulting from TB infections are recorded compared to developed regions where sophisticated diagnosis equipment is readily available.

Accurate and timely diagnosis of TB is ultimately essential to treating and eradicating this global epidemic disease. Identifying the extent of TB infection as either latent or active is fundamental as these conditions require different treatment procedures. The issue of resistance to drugs makes finding

a cure for TB more problematic as most of the available drugs are becoming ineffective and hindering the goal of extinguishing the infection [9]. Diagnosing TB is sometimes tricky in cases where the patients exhibit symptoms that are similar to other illnesses and scenarios. Moreover, where the patients exhibit co-infections such as TB + HIV makes it even more problematic as the presence of active TB could be masked, resulting in an undetected and untreated case which increases the likelihood of death in patients [2].

Recently, classification methods have become popular for screening various abnormalities in medical imaging as the utilization of an efficient classification tool is essential for improving the quality of diagnosis while reducing the time taken to diagnose [10]. There are several means of screening for TB in a patient, such as a Chest X-Ray (CXR), Tuberculin Skin Test (TST), Sputum Microscopy, and Mycobacteria Growth Indicator Tube (MGIT), among others [11]. Still, the CXR is a less expensive way of diagnosing TB manifestation [9], [12]. Regrettably, interpreting the CXR is dependent on the skill and expertise of a radiologist, and it is subject to misdiagnosis [13], [14]. Diagnosing many patients with TB symptoms requires being x-rayed and screened for the type of TB (either latent or active) to make sure that appropriate therapy is administered.

Furthermore, manually diagnosing a large number of patients is a laborious and time-consuming task that could result in misdiagnosis. In most developing regions, for instance, in Africa, where the resources required to undertake adequate diagnosis are lacking, it is a significant challenge to curb the TB epidemic. Consequently, developing Computer-Aided Detection (CAD) systems to detect TB infection in CXR automatically is a promising way of reducing diagnosis errors and ultimately increasing the quality of diagnosis.

The rationale for this review study is to:

- Present a comprehensive background that serves as a guide for the application of deep learning in the development of an existing computer-aided diagnostic (CAD) system for TB detection;
- Highlight the strengths and weaknesses of current state-of-the-art deep learning architectures.
- Provide detailed information on the various CXR dataset, and finally
- Identify future directions that may further improve analyzing medical imaging and developing efficient CAD for diagnosing TB and other pulmonary diseases.

This study contains recent and relevant details that are specifically useful for researchers interested in applying deep learning architectures to real-life problems, academia, and governments interested in the extent of effort invested in developing CAD for solving the global TB epidemic.

Manuscript received July 28, 2021; revised July 26, 2022.

Mustapha Oloko-Oba is a PhD candidate at the School of Mathematics, Statistics and Computer Sciences, University of KwaZulu-Natal, Durban, South Africa e-mail: 219098624@stu.ukzn.ac.za.

Serestina Viriri is a Professor of Computer Science at the School of Mathematics, Statistics and Computer Sciences, University of KwaZulu-Natal, Durban, South Africa. e-mail: viriris@ukzn.ac.za.

## II. SURVEY METHODOLOGY

This section discusses the comprehensive procedures for the articles reviewed in this study, including article database, search keywords, and standards for inclusion.

### A. Databases

The databases utilized for searching articles were IEEE Xplore, Scopus, and Science Direct, basic and advanced searches for related journals, conference proceedings and books in the computer science and medical domain. The focus was on the journals and conference proceedings articles because they often contain recent research discoveries related to the study.

### B. Search Keywords

Searches were performed across the three databases using the following search terms: Tuberculosis, Machine Learning, Deep Learning, Chest X-Ray, Diagnosis, Segmentation of Lung Fields, Computer-Aided Detection, and Classification.

### C. Standards for Inclusion/Exclusion

- Article language is an important criterion considered in this study. The articles included were written entirely in English, while papers presented in other languages were excluded.
- Articles selection was based on a comprehensive search for publications in the medical domain related to pulmonary TB abnormalities and computer science domain concerning (deep learning and machine learning) methods.
- The articles reported cover the period between 2000 to 2020. This period was suitable for exploring the research evolution and findings on the conventional and state-of-the-art methods of TB diagnosis.
- Articles that did not sufficiently report methods and detail results in terms of performance accuracy were excluded.
- Articles were searched using the appropriate keywords as listed above. The search results were then scanned to filter topics related to the study. An overview reading of the abstract, methods, and conclusion was followed to further screen relevant articles for full-text reading and better understanding.

Three hundred seventy-one (371) articles were subjected to title and abstract scans, out of which 200 papers were found suitable for full-text reading. The detailed reading further streamlined the paper to 160, which were finally included in the study.

## III. CONVENTIONAL TUBERCULOSIS DIAGNOSIS TEST

Before the advent of deep learning in diagnosing TB from CXR, several methods were used in screening TB manifestation in patients. These methods are briefly discussed below:

### A. Tuberculin Skin Test

Tuberculin Skin Test (TST) is one of the standard methods of diagnosing TB. In this method, a small amount of Tuberculin which contains some inactive TB protein is injected into the forearm skin. The patient will then return after 2-3 days to observe if there is a reaction or not. Mostly, if the patient has some swelling or a hard lump on the arm, this indicates the presence of TB bacteria in the body; otherwise, the patient is considered negative for TB bacteria when there is no reaction in the arm. TST is vital in identifying the presence of TB bacteria [15] but cannot determine the state of the TB infection as either latent or active TB [2].

### B. Interferon Gamma Release Assays

Interferon Gamma Release Assays (IGRA) is a TB examination procedure that is dependent on blood to measure the patient immune response to TB bacteria. In the IGRA screening, interferon-gamma is released in the white blood cells of an infected individual when combined with TB protein derivative [16]. Just like the TST, IGRA screening is also unable to distinguish latent TB from active TB but is more explicit than the TST because it is not affected by prior Bacillus CalmetteGurin vaccines [17].

### C. Smear Microscopy

Smear Microscopy involves placing sputum (a mixture of mucus, spit, saliva) under the microscope for a period of six weeks for the detection of mycobacterial growth. This method is one of the primary means of TB diagnosis in a low-income region where TB is most prevalent [18]. This method is mostly inaccurate due to low sensitivity in co-infected cases. It has a low track report in paediatric TB and extrapulmonary TB and takes too long to give a result [19], [2].

### D. GeneXpert/Xpert MTB/RIF

GeneXpert/Xpert MTB/RIF is an amplification examination for detecting mycobacteria TB (MTB) and resistance to a TB drug known as Rifampicin. The Xpert MTB/RIF is an initial diagnostic screening for TB infections and diagnoses faster and better than the Smear Microscopy. Still, it is very expensive and requires a constant electricity supply [20] which makes it a challenge in developing regions where stable electricity is lacking.

### E. Mycobacteria Growth Indicator Tube

The Mycobacteria Growth Indicator Tube (MGIT) developed by Becton Dickinson [21] is used to screen the possibility of TB bacteria growing when subjected to different TB drugs to determine if the TB bacteria are resistant to a particular drug or not. This is an expensive screening method; it requires sufficient testing equipment and skilled personnel as it needs to be isolated in a laboratory [22], [23].

Another TB drug-resistant screening method that requires being isolated in the laboratory is the Genotype MTBDR and INNO-LiPA Rif TB [24]. This testing technique also requires sufficient equipment and skilled personnel, as in the case of MGIT.

All the generally known TB diagnostic approaches have limitations, especially in co-infection cases such as TB and HIV. Hence the continuous need to ensure the rapid reduction in the mortality rate recorded and total eradication of the TB epidemic [1] in which early detection is a decisive factor [9].

The constraints of the existing TB diagnosis techniques contribute to diagnostic delays resulting in severe consequences for the global efforts of controlling and eradicating the epidemic [25]. CXR can be employed as both a measurement and screening medium to identify all the various manifestations and abnormalities with respect to pulmonary infections [26].

The advent of the Computer-Assisted Detection (CAD) system for detecting TB manifestation is a promising tool that will assist health care centres in eliminating the delay arising from the conventional methods of diagnosing patients and provide accurate diagnoses in the developing regions where TB is most prevalent.

#### IV. CHALLENGES ASSOCIATED WITH TB DIAGNOSIS IN CHEST X-RAY

Delay in screening is the first challenge that impacts the quality of diagnosis. Screening delay is a critical factor that can diminish the quality of diagnosis and contribute hugely to the high rate of death associated with TB. Delays could be patient-based (from the onset of clinical symptoms until the initial visit to the medical facility), or health personnel based (from the patient's initial visit to a medical facility until the diagnosis is established). Inadequate screening equipment, high cost of screening, and lack of skilled medical personnel are among other diagnostic delays that are mostly observed in high TB burden regions such as Africa and Asia [2]. The global impact of TB liability is increasing in developing regions compared to developed areas. Individuals that show TB manifestation can be clinically categorized into latent and active TB. The latent (dormant) TB is quickly advanced into active TB when left untreated or detected.

The common radiological entities of TB manifestations on CXRs are:

- **Miliary Pattern:** appears in the lungs in a sand-like formation affecting around 1% - 7% TB infected persons. The miliary pattern usually displays manifestation between 6 months from the onset of exposure [27], [28].
- **Adenopathy:** results in enlargement of the nodes. It usually affects the right-side region of the lung and is mostly observed in children (up to 83%-96%) as compared to adults (between 10%-43%) [29].
- **Pleural Effusion:** This is excessive fluid building up within the medial and lateral regions. The pleural effusion usually produces a small amount of fluid that acts as a lubricant that facilitates breathing but once infected, it produces excess fluid [30].
- **Airways Enlargement:** is usually visible as tabular rings extending from the lung [31].
- **Airspace Consolidation:** is a condition that is visible in the lobe as opacity; it is often diagnosed as pneumonitis [32].

Most of the attributes associated with TB infection may also be present in other diseases. In some cases, the chest screening of an infected patient looks perfect to the human

eye. At the same time, some may exhibit faint abnormalities that can only be spotted by a skilled radiologist [33].

As reported in [26] CXR is a vital screening procedure in detecting abnormalities as well as the manifestation of TB in patients. CXR can be employed as a guide to determine when additional screening of infected individuals is required and provide reassuring proof to confirm TB manifestation when the bacteriologic outcome is undetermined or uncertain. Interpreting CXR as both measurement and screening procedure is of utmost importance.

Screening is carried out to identify any abnormalities relating to TB. However, it is pertinent to include both TB specific and non TB CXR in the screening procedures to improve the quality of the result. The utilization of computer-aided detection (CAD) systems in analyzing CXR can enhance the quality, timeliness and accuracy of diagnosis, thereby surpassing manual human interpretation [26].

Although CXR has some limitations, such as requiring skilled professionals for proper screening exercise and interpretation, standard equipment with stable power (electricity), and ionizing radiation exposure, recent efforts such as decreasing the dose of radiation, improving the archiving facility, advancing the quality of image, utilization of CAD, and harmonizing scan interpretation and reports have assisted in maintaining CXR as a vital tool in detecting TB cases.

#### V. STATE-OF-THE-ART CONVOLUTIONAL NEURAL NETWORK ARCHITECTURES

In this section, we present prominent Convolutional Neural Network (CNN) models capable of extracting and learning distinctive features/patterns from images. These models have been successfully and widely utilized for various tasks such as diagnosis, recognition, classification, prediction, estimation, etc. The AlexNet, GoogLeNet, VGGNet, ResNet, SqueezeNet, Xception, CapsuleNet, and ZFNet architectures are described below.

##### A. AlexNet Architecture

In 2012, Krizhevsky et al. [34] presented the AlexNet structure, which is made up of five successively convolutional layers and three fully connected layers. The architecture achieved the topmost performance in the ImageNet Large Scale Visual Recognition Challenge (ILSVRC-2012) competition against all other competitors. Their achievement brought about a fundamental advancement in machine learning for recognition and classification tasks, which led to increased interest in the deep learning domain. The AlexNet architecture employed augmentation and dropout techniques to drastically reduce overfitting and was the first to implement the Rectified Linear Unit (ReLU) activation function. AlexNet is, however, computationally expensive. Figure 1 shows a representation of the AlexNet structure.

##### B. Visual Geometry Group (VGGNet) Architecture

The Visual Geometry Group (VGG) was presented by [35] and emerged as the runner up after GoogLeNet in the ImageNet ILSVRC 2014 classification challenge. The VGG structure consists of convolutional layers which utilize the ReLU activation function followed by a max-pooling layer and then the fully connected layers that also utilize

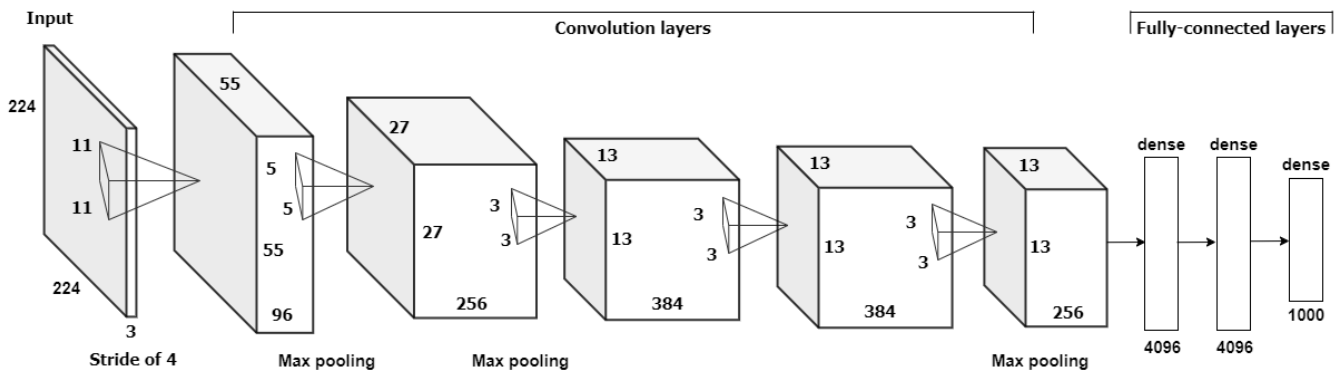


Fig. 1. The AlexNet Architecture. Figure reproduced from [34]

the ReLU activation function except for the final layer, which uses Softmax activation function for classification. This model exhibits that the depth of a network is important for obtaining better performance accuracy. The VGGNet uses 3x3 kernel size filters to modify the AlexNet 11x11 and 5x5 filters. There are different variants of VGG like VGG-11, VGG-16, and VGG-19, all of which have the same number of fully connected layers but different convolutional layers specific to each variation. This model has established effectiveness as evident in [36], [37], [38] for TB detection with better generalization even though it is time-consuming when training from scratch, sluggish to train and the weights of the model are quite large. See Figure 2 for the VGGNet architecture.

### C. GoogLeNet Architecture

GoogLeNet, otherwise known as Inception V1, was presented at the 2014 edition of the ImageNet Large-Scale Visual Recognition Challenge by [39] and won the best architecture concerning detection and classification of images. The architecture consists of 22 deep network layers that aim to reduce previous architectures' computational complicity to achieve improved detection and classification of objects.

The 22 layers depth of GoogLeNet learns faster and surpasses the previous architectures. However, it has lower computation and lesser network parameters of about 7 million compared to VGG-19's 138 million and AlexNet's 60 million. GoogLeNet has successfully been used in [40], [41], [36] for detecting TB from CXR. The GoogLeNet architecture is presented in Figure 3.

### D. ResNet Architecture

Residual Network, popularly known as ResNet, was presented by [42] to resolve the vanishing gradient issue and simplify the complexity of deeper networks. Rather than learning the unreferenced functions, the ResNet framework distinctly recomposes layers as learning residual functions regarding the layer's input. The network offers the idea of identity mappings and residual sections and consists of different residual blocks.

The residual section consists of two parts: firstly, an alternative links the input to the second part and then convolutions with an activation part. The result of the residual network

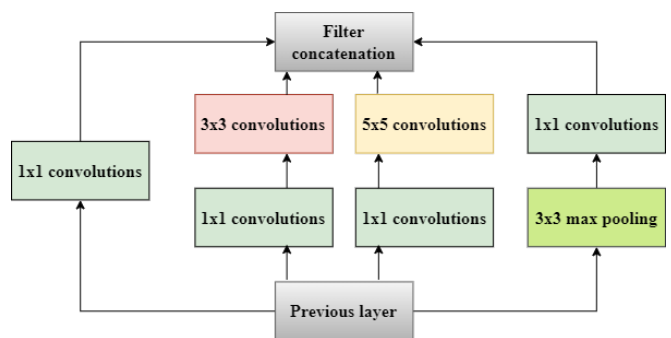


Fig. 3. The GoogLeNet Inception module with reduced dimensionality. Figure reproduced from [39]

won the 2015 edition of the ILSVRC classification challenge. ResNet is easier to optimize and attains better accuracy from a deeper network using the Deeper Bottleneck structure, an extension of the residual section. Nevertheless, ResNet takes lots of time to train and is quite expensive computationally. ResNet has a deep variant for difficult tasks and a shallow variant for simple tasks. Other variations of residual models are proposed in [43], [44], [45]. Figure 4 shows a residual network architecture.

### E. SqueezeNet Architecture

A mini CNN model named SqueezeNet was proposed by [46] to achieve the same accuracy level as the robust architectures rather than only focusing on increased accuracy with deeper models. The authors believed that building mini architectures were more feasible to deploy across networks with little memory size, required smaller bandwidth to ease exporting, and limited communication during training across servers. SqueezeNet architecture is less than 0.5-megabyte model size and has fewer parameters yet attained the same accuracy level with a deeper network AlexNet on the same ImageNet datasets.

The SqueezeNet architecture is developed out of fire modules. The architecture begins with inputting an image into the convolutional layer, which is passed through 8 sequential fire modules while the number of filters per module gradually increases. Then the process is moved to another convolutional layer.

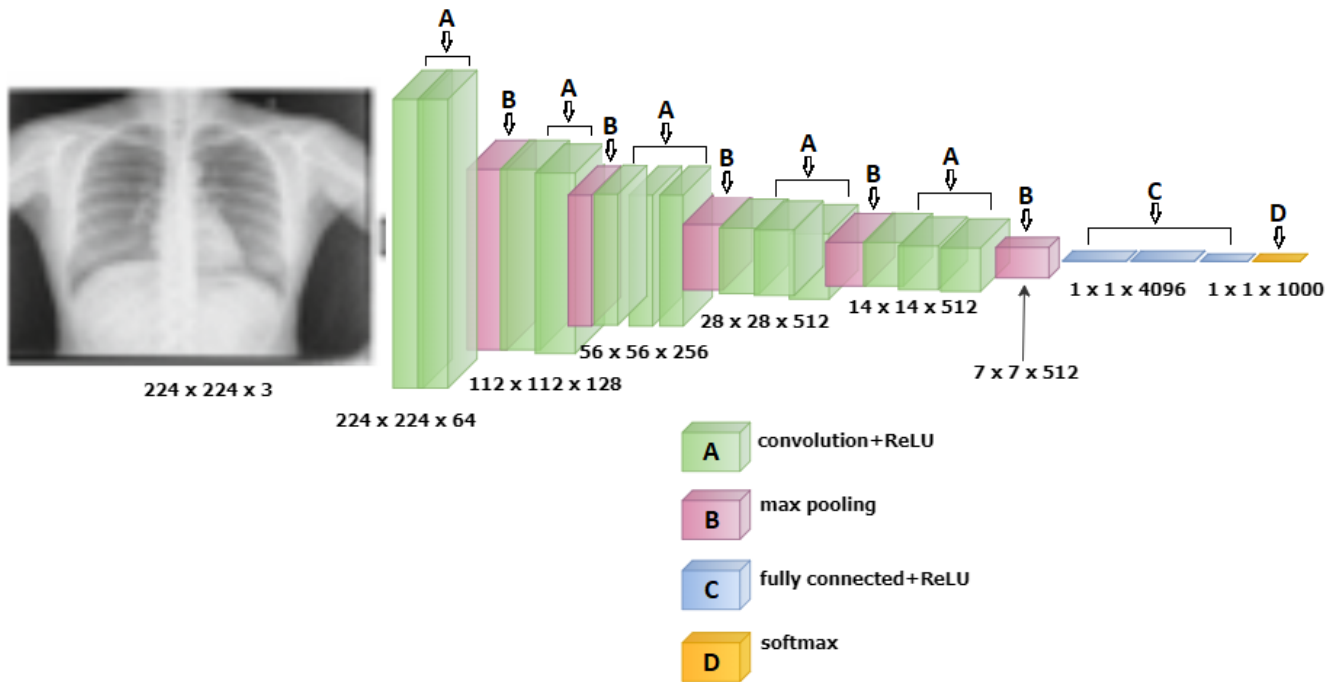


Fig. 2. The VGGNet Architecture. Figure reproduced from [35]

Max-pooling operation is performed in the model with strides of 2 at different intervals as shown in Figure 5. Global average pooling replaces the fully connected layers before passing them on to the Softmax classifier. Although SqueezeNet can achieve better accuracy, the small nature of the architecture will impact its generalization performance.

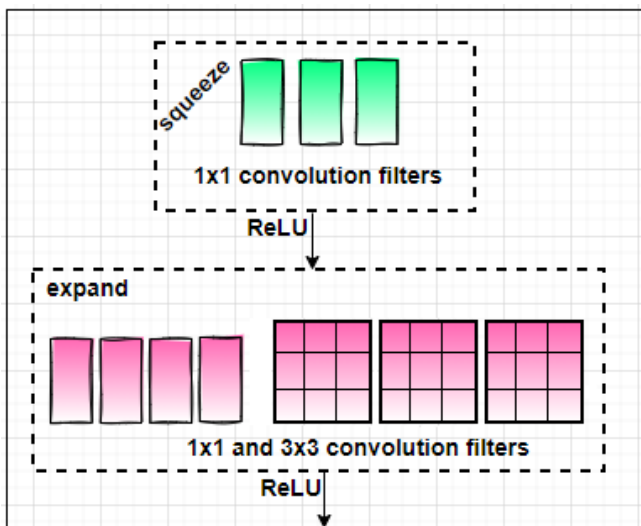


Fig. 5. SqueezeNet fire module Architecture. Figure reproduced from [46]

**F. Xception Architecture**

Xception, which stands for Extreme Inception, is entirely dependent on the depthwise separable convolution [47] and

is presented in [48] with the assumption that spatial correlation and cross channels correlations mapping in the feature maps of CNNs can be completely decoupled. The feature extraction part of the Xception model is composed of 36 convolutional layers followed by logistic regression layers. The layers within the Xception model are arranged into 14 layers consisting of linear residual connections around them, excluding only the first and last modules. The linear stack with residual connections mode makes defining and modifying the Xception model easier than the Inception V3. The experimental results of the Xception model showed exceptional performance over the Inception V3 model on a larger JFT dataset. Still, they slightly improved the ImageNet datasets upon which the Inception V3 model was initially built. The Xception model is presented in Figure 6.

**G. CapsuleNet Architecture**

CapsNet architecture presented in [49] is a shallow network that consists of two convolutional layers and one fully convolutional layer. The first convolutional layer of CapsNet changes pixel intensities to the task of local feature detectors that are further pushed as inputs to the primary capsule modules and then passed to the second convolutional layer before passing on to the DigitCaps. The idea behind CapsNet is to add a capsule module to CNN; the output from these capsules is then used to form a steady representation for greater capsules to output a vector. CNN does not consider the relationship between objects and affine transformation, which is the strength of CapsNet. Training CapsNet from scratch on the MultiMNIST dataset attained a higher test classification accuracy than baseline convolutional structures and performed well on the CIFAR-10 dataset. Also, in [50],

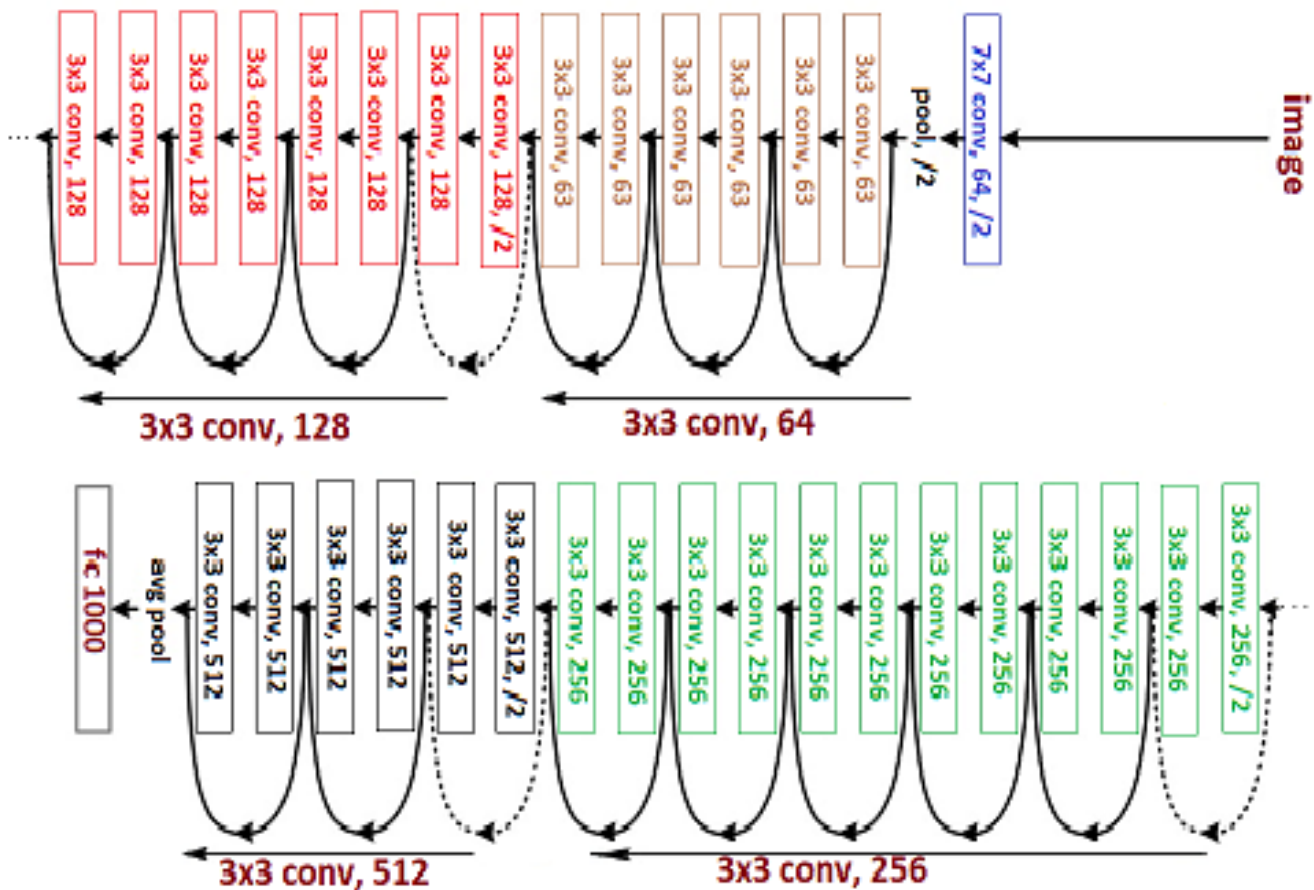


Fig. 4. A ResNet Architecture with 34 parameter layers. Figure reproduced from [42]

the authors employed customized CapsNet along with VGG-16 and AlexNet for classifying TB in CXR. The result showed that the CapsNet structure outperformed VGG-16 and AlexNet with respect to predicting affine images. The general architecture of CapsNet is presented in Figure 7 while Figure 8 is a customized CapsNet architecture for TB detection.

#### H. ZFNet/Clarifai Architecture

In the 2013 edition of the ImageNet classification challenge, the authors in [51] present ZFNet, an eight layers model which improved on the AlexNet architecture. ZFNet showed significant improvement by tweaking the AlexNet model. They introduced a visualization technique that provided insight into the intermediate layers to identify problems of the model. The modifications that resulted in improving the classification errors were (a) substituting the 11x11 filters in the AlexNet first convolutional layer with a 7x7 filters and (b) utilizing strides of two as a substitute for the original four strides. These modifications were essential to the ZFNet architecture for outperforming the AlexNet on the same ImageNet benchmark dataset and won the 2013 ILSVRC challenge. The ZFNet also showed better generalization and outperformed modern results on both CalTech-101 and 256 datasets.

Other architectures include FractalNet [52], Densely Connected Network (DenseNet) [53], Network in Network (NiN) [54], and Faster R-CNN [55]. A detailed description of the current state-of-the-art architectures is presented in Table I

#### VI. OVERVIEW OF PROMINENT CXR DATASETS

Data is crucial for the development of algorithms required to solve life-threatening diseases, including TB, which is one of the leading causes of death worldwide [1]. The various prominent CXR datasets employed in training and testing TB detection algorithms are described below. These datasets are made available to the research communities to foster state-of-the-art research into finding lasting solutions to the early diagnosis of TB manifestations.

##### A. Montgomery County Dataset

The Montgomery County (MC) CXR dataset is a TB specific dataset made available by the National Library of Medicine in conjunction with the Department of Health Services Maryland, U.S.A., for research intent. This dataset is composed of 58 abnormal samples and 80 normal samples. The naming of each image ends with either "0" denoting normal sample or "1" denoting abnormal sample. All samples are 4020 x 4892 pixels and are available in portable network graphic (png) file format. This dataset is accompanied by

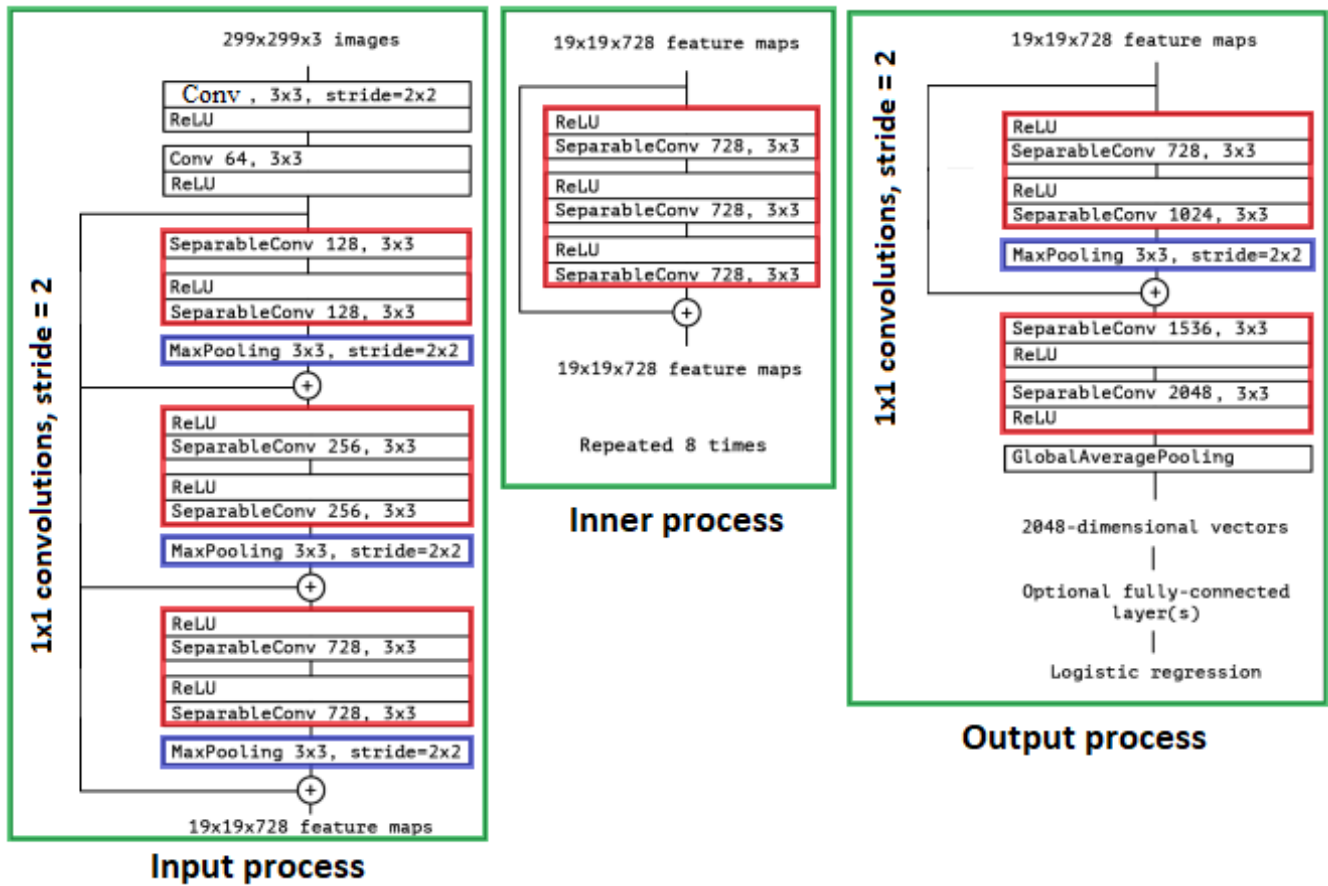


Fig. 6. The Xception Architecture. Figure reproduced from [48]

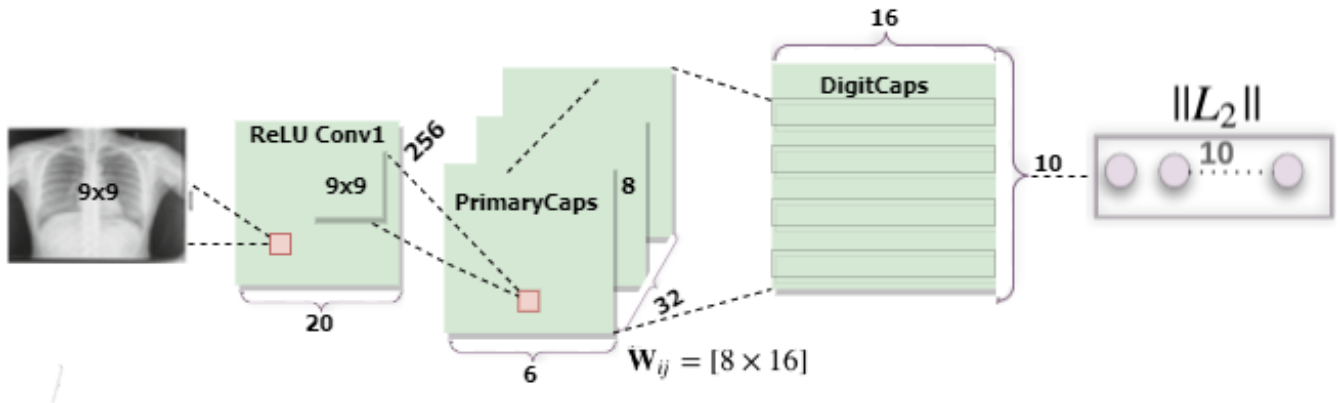


Fig. 7. A simple 3 layers CapsNet Architecture. The occurrence of every class is represented in DigitCaps layer that is utilized for computing classification loss.  $W_{ij}$  represents the weights between primary capsule layer and DigitCaps layer. Figure reproduced from [49]

clinical readings that give details about each sample concerning sex, age, and manifestations. The MC dataset is accessible from the NIH website <https://lhncbc.nlm.nih.gov/publication/pub9931>.

**B. The Shenzhen Dataset**

The Shenzhen dataset is specific to TB and is publicly available for research. It is made up of 336 abnormal (positive) samples and 326 normal (negative) samples. The naming of each image ends with either a 0 denoting a normal sample or a 1 representing an abnormal sample.

All images are approximately 3000 x 3000 pixels saved in portable network graphic (png) file format. This dataset is accompanied by clinical readings that give details about each of the samples with respect to sex, age, and diagnosis. The Shenzhen dataset is accessible from the NIH website.

**C. JSRT Dataset**

The Japanese Society of Radiological Technology puts together the JSRT dataset in collaboration with the Japanese Radiological Society. The dataset comprises 247 CXR, 93 are

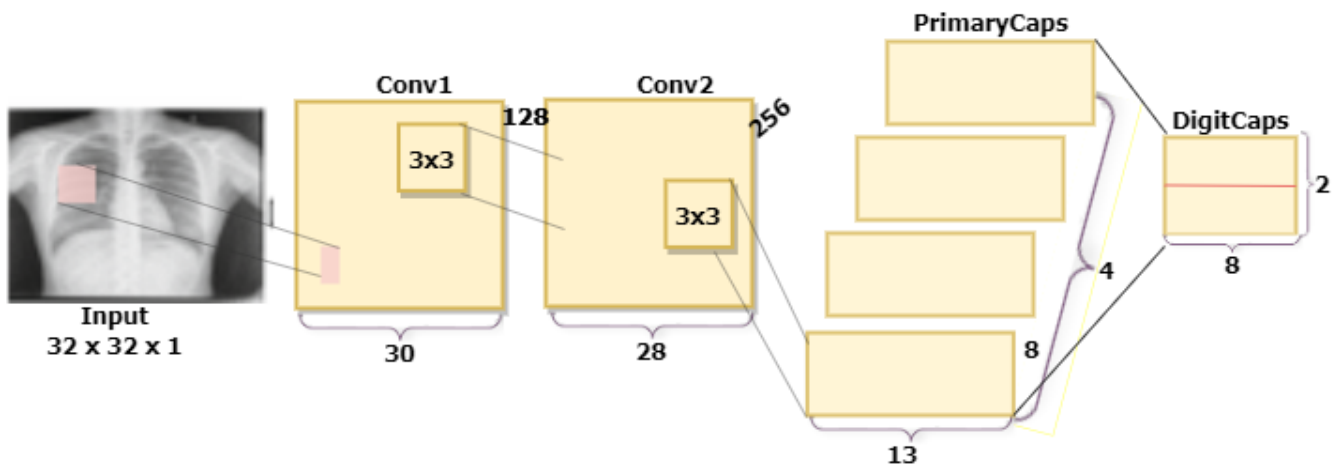


Fig. 8. CapsNet architecture for TB detection. Figure reproduced from [50]

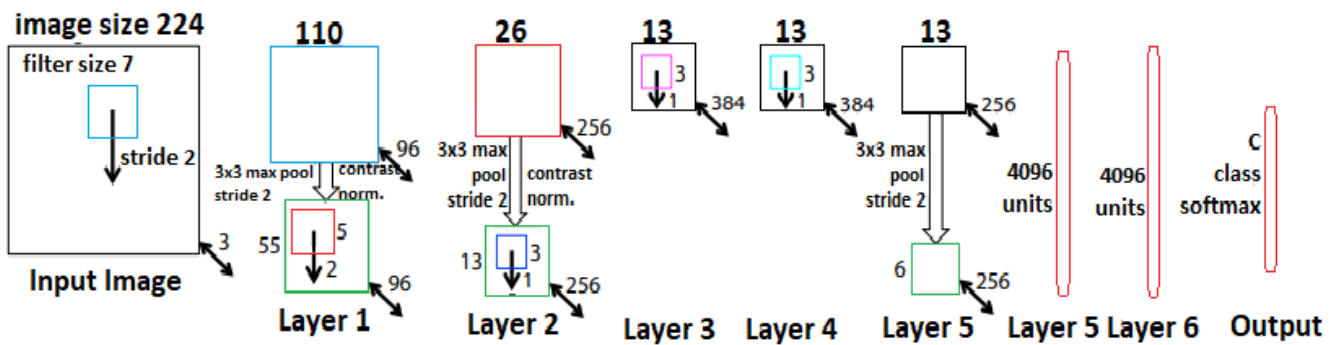


Fig. 9. Architecture of ZFNet. Figure reproduced from [51]

without lung nodules, and 154 are with lung nodules. The images are  $2048 \times 2048$  pixels in a universal image format (uif). This dataset also has additional patient information such as gender, age, diagnosis, nodule location diagram, degree of subtle, and X and Y coordinates of nodules. The JSRT dataset can be requested from the Japanese Society of Radiological Technology website <https://db.jsrt.or.jp/eng.php>.

#### D. Indiana (OpenI) Dataset

The Indiana CXR dataset was collected from two hospitals by the Indiana University Network for Patient Care. The dataset comprises 3996 posterior-anterior CXR images of varying sizes ranging from 1024 pixels minimum dimension to a maximum dimension of 4248 pixels. It contains 1526 normal images and 2470 abnormal images of 10 different manifestations, including pleural effusion, cardiomegaly, opacity, etc. and is accompanied by radiologist reports. The dataset can be downloaded at <https://openi.nlm.nih.gov/faq#collection>.

#### E. The Peruvian Dataset

The Peruvian dataset is provided by the Socios en Salud, Partners In Health in Lima, Peru [41]. It consists of 4701 CXR images, out of which 453 are normal, i.e. healthy, while 4248 are abnormal class, i.e. unhealthy with various manifestations. The manifestations are classified into six: cavitation lymphadenopathy, miliary pattern, alveolar infiltration, ghon focus, and others. The images are stored in JPEG file format.

#### F. KIT Dataset

The KIT is a TB specific dataset and is made up of 10848 CXR images provided by the Korea Institute of TB under the Korean National TB Association (KNTA), South Korea [56]. There are 7020 normal samples and 3828 abnormal samples. The images are provided in the Digital Imaging and Communications in Medicine (DICOM) file format.

TABLE I: Description of state-of-the-art CNN architectures used in Tuberculosis diagnosis.

Architecture	#Parameters	#Layers	Strenghts	Weaknesses
AlexNet [34]	62,369,152	8 Layers	<ul style="list-style-type: none"> <li>• AlexNet is a milestone CNN architecture for image classification whose success at the 2012 ImageNet challenge brought fundamental advancement and increased interest in the deep learning domain.</li> <li>• It was the first to implement the ReLU activation function.</li> <li>• It employed dropout and label-conserving transformations to reduce overfitting issues.</li> </ul>	<ul style="list-style-type: none"> <li>• It is computationally expensive.</li> <li>• Its performance is outperformed not only by deeper models like GoogleNet and ResNet but also ZFNet with the same number of layers.</li> </ul>
VGGNet [35]	143,557,700	The layers of VGGNet varies depending on the variant. VGGNet has layers such as 19, 16, and 11.	<ul style="list-style-type: none"> <li>• It shows better generalization on a new dataset.</li> <li>• It is popular and widely used for features extraction in computer vision tasks.</li> </ul>	<ul style="list-style-type: none"> <li>• It has too many parameters which can be challenging to handle</li> <li>• The weight is quite large.</li> <li>• It is slow to train.</li> </ul>
GoogLeNet [39]	6,797,700	22 layers.	<ul style="list-style-type: none"> <li>• GoogleNet trains faster than VGG</li> <li>• It has a small weight.</li> <li>• The error rate is low.</li> <li>• The network learns faster and more efficiently while increasing network depth.</li> </ul>	<ul style="list-style-type: none"> <li>• The network model is deeper and more complex than AlexNet, hence will require more computational power.</li> </ul>
ResNet [42]	11,700,000 21,800,000 23,900,000	ResNet has variants with different layers such as 18, 34, 50, e.t.c.	<ul style="list-style-type: none"> <li>• ResNet resolve the vanishing gradient issue using shortcut connections.</li> <li>• It encourages feature reuse and strengthen feature propagation.</li> <li>• Its computationally more efficient than VGGNet.</li> <li>• It uses few filters that lead to fewer model complexity.</li> </ul>	<ul style="list-style-type: none"> <li>• The model is computationally expensive with large network depth.</li> <li>• It also takes a lot of time to train the model thereby requires high computational power.</li> </ul>

*Continued on next page*

TABLE I – *Continued from previous page*

Architecture	#Parameters	#Layers	Strengths	Weaknesses
SqueezeNet [46]	1,248,424	14 layers	<ul style="list-style-type: none"> <li>• SqueezeNet architecture is less than 5 megabyte model size and cautiously reduce the number of parameters yet attained same accuracy level with a deeper network AlexNet on same ImageNet datasets.</li> <li>• SqueezeNet proves that mini architectures are more feasible to deploy across networks with little memory size, it requires small bandwidth to ease exporting over hardware, as well as limit communication during training across servers.</li> </ul>	<ul style="list-style-type: none"> <li>• SqueezeNet is not included in the Keras core library.</li> <li>• likewise, the architecture's mini nature will impact its performance on generalization.</li> </ul>
Xception [48]	22,855,952	71 layers	<ul style="list-style-type: none"> <li>• It is entirely based on depthwise separable convolutions.</li> <li>• The architecture is easier to define and modify as a result of the linear stack mode with residual connections.</li> <li>• Xception outperforms ResNet, VGGNet, and Inception V3 architectures on the same ImageNet datasets.</li> <li>• It decoupled spatial and cross channels correlations mapping in the feature maps to gain computational efficiency.</li> </ul>	<ul style="list-style-type: none"> <li>• High computational cost</li> <li>• Xception is marginally slower compared to Inception modules.</li> </ul>

*Continued on next page*

TABLE I – Continued from previous page

Architecture	#Parameters	#Layers	Strenghts	Weaknesses
CapsNet [49]	8,200,000	3 layers	<ul style="list-style-type: none"> <li>• Capsule represents neurons better.</li> <li>• It is very robust to affine transformation because DigitCaps learns more robust representation for each class than the conventional CNN.</li> <li>• It uses neural activities that vary as view-points rather than striving to eliminate view-points variations from activities.</li> <li>• CapsNet is good at dealing with segmentations.</li> <li>• It has very few network parameters (8.2M)</li> </ul>	<ul style="list-style-type: none"> <li>• CapsNet is not popoular yet. i.e, it has not been sufficiently evaluated on large datasets.</li> <li>• Computing and implementation of CapsNet is highly demanding.</li> </ul>
ZFNet [51]	50,777,640	8 layers	<ul style="list-style-type: none"> <li>• ZFNet outperformed AlexNet. It Tweak the AlexNet by substituting 11x11 filters with 7x7 and used a stride of 2 instead of 4.</li> <li>• It introduced state of the art technique of visualizing activities within the model.</li> <li>• It improves overall recognition precision.</li> <li>• It generalized well and also outperformed modern results on CalTech-101 and 256 datasets.</li> </ul>	<ul style="list-style-type: none"> <li>• Requires extra processing information for visualization.</li> </ul>

### G. Belarus Dataset

The Belarus dataset is put together and maintained by Belarus TB Public Health. The dataset consists of 304 CXR images, which are entirely positive for TB with different abnormalities such as miliary pattern, pleural effusion, and cavitation manifestations. Out of the 304 images, 194 are associated with male patients, while 110 are associated with female patients. The CXR images vary in size from 2248 x 2248 to 2724 pixels and are stored in Digital Imaging and Communications in Medicine (DICOM) file format. The dataset is usually requested from the Belarus TB portal but was unavailable at the time of this report. The images were used in [40], [57].

### H. India Dataset

The India dataset is obtained from private hospitals in India. The set comprises 397 CXR images with different dimensions like 1772 x 1430 pixels, 2010 x 1572 pixels, and 2446 x 2010 pixels, respectively, in a 12-bit grayscale. The images are 0.175mm pixels spacing in horizontal and vertical directions. The India datasets were reported in [58].

### I. CheXpert Dataset

CheXpert [59] is a huge CXR dataset collected at Stanford Hospital in California between the years 2002 to 2017. The dataset is composed of 224,316 CXR images along with their associated radiological interpretations from 65,240 patients and is labelled as positive, negative, and uncertain for the presence of 14 clinical observations. The dataset also features labelled radiologist tests and validation sets, which serve as standard references and expert scores evaluating distinctive models. The dataset is available for downloading after accepting the CheXpert research use agreement by the Stanford University School of Medicine to complete the registration form. The download link, which may not be shared with others, will be sent to the registered email for downloads. The agreement form to request the CheXpert datasets can be found at the Stanford ML Group website <https://stanfordmlgroup.github.io/competitions/chexpert/>.

### J. MIMIC-CXR Dataset

The MIMIC-CXR dataset [60] is sourced from the Beth Israel Deaconess Medical Center between 2011 and 2016. The dataset consists of 377,110 CXR originally in Digital Imaging and Communications in Medicine (DICOM) file format and then exported in the JPEG standard format, which is now MIMIC-CXR-JPG that is entirely derived from the MIMIC-CXR dataset, and aims to provide a convenient processed version of MIMIC-CXR, as well as provide a standard reference for image labels and data splits. The dataset is available to all researchers for use after completing a data use agreement which states that the researcher will not attempt to re-identify the patients because all the images are de-identified to protect patient's privacy, the data is not shared with others, and relevant codes emanating from any publications for the use of the dataset be made available. A detailed description of the dataset and download can be found on the PhysioNet website <https://physionet.org/content/mimic-cxr-jpg/2.0.0/>.

### K. NIH Dataset

The NIH CXR [61] dataset was provided by the National Institute of Health, Bethesda, MD, USA and consists of 108,948 de-identified CXR, including radiological reports saved in PNG format. The images are labelled with the presence of 8 pathologies as follows: Mass, Cardiomegaly, Pneumothorax, Effusion, Nodule, Atelectasis, Pneumonia, and Infiltration or otherwise labelled as normal if no manifestation is observed. Some images can have one or more pathology. This dataset is often referred to as chest x-ray8 or chest x-ray14 and is available for downloading at the NIH website <https://nihcc.app.box.com/v/ChestXray-NIHCC> with no restrictions for use.

Apart from the prominent dataset mentioned above, other independent datasets have been utilized for research. Some of these datasets include the TB specific datasets of the Sehatmand Zindagi Healthy Life Centres [62], CXR scans from the University of Alberta Hospital [63], Imagine dataset of the Seoul National University Hospital [64], the Boramae Medical Center datasets, Daejeon Eulji Medical Center datasets, and the Kyunghee University Hospital at Gangdong datasets[64].

Table VI-K presents a brief summary of the datasets studied in this paper while Figure 10 show the datasets frequency of use in publications

### L. Summary

All of the above datasets are de-identified to protect the patients' privacy. In other words, the identity of the patients is not disclosed. Most of the CXR datasets are accompanied by radiological interpretations of observed manifestations. The Montgomery and the Shenzhen, for instance, also have a ground truth of the images to assist researchers in a segmentation task. The datasets are freely available to researchers for various research tasks such as segmentation of the lungs, detecting pulmonary abnormalities, etc. The MIMIC and CheXpert, for instance, require researchers to complete a data users agreement form before the datasets can be downloaded for use.

## VII. TECHNICAL ADVANCES AND THE NEED FOR TIMELY AND CORRECTLY DIAGNOSIS OF TB

In spite of the various efforts to control the TB epidemic, the rate of detecting active TB in developing regions remains a concern. As reported in [65], almost half of the cases of TB remain undiagnosed in the African regions of the World Health Organization (WHO), where only about 60% of cases of TB are detected, leaving about 40% of cases undetected.

In most TB + HIV co-infection regions, fewer than 18 out of 50 cases are detected. Differentiating and detecting latent or active TB in HIV co-infection cases in developing regions remains a serious problem. Also, out of about 500,000 new multi-drug resistant TB infected individuals estimated yearly, only 7% of cases are detected after a lengthy delay before diagnosis [66].

The optimal diagnosis of TB is faced with the crucial and logistic difficulty of purchasing and providing the needed equipment, especially in the developing nations, when compared to the case of HIV, where the maximum effort was involved in curbing the HIV menace with huge investments

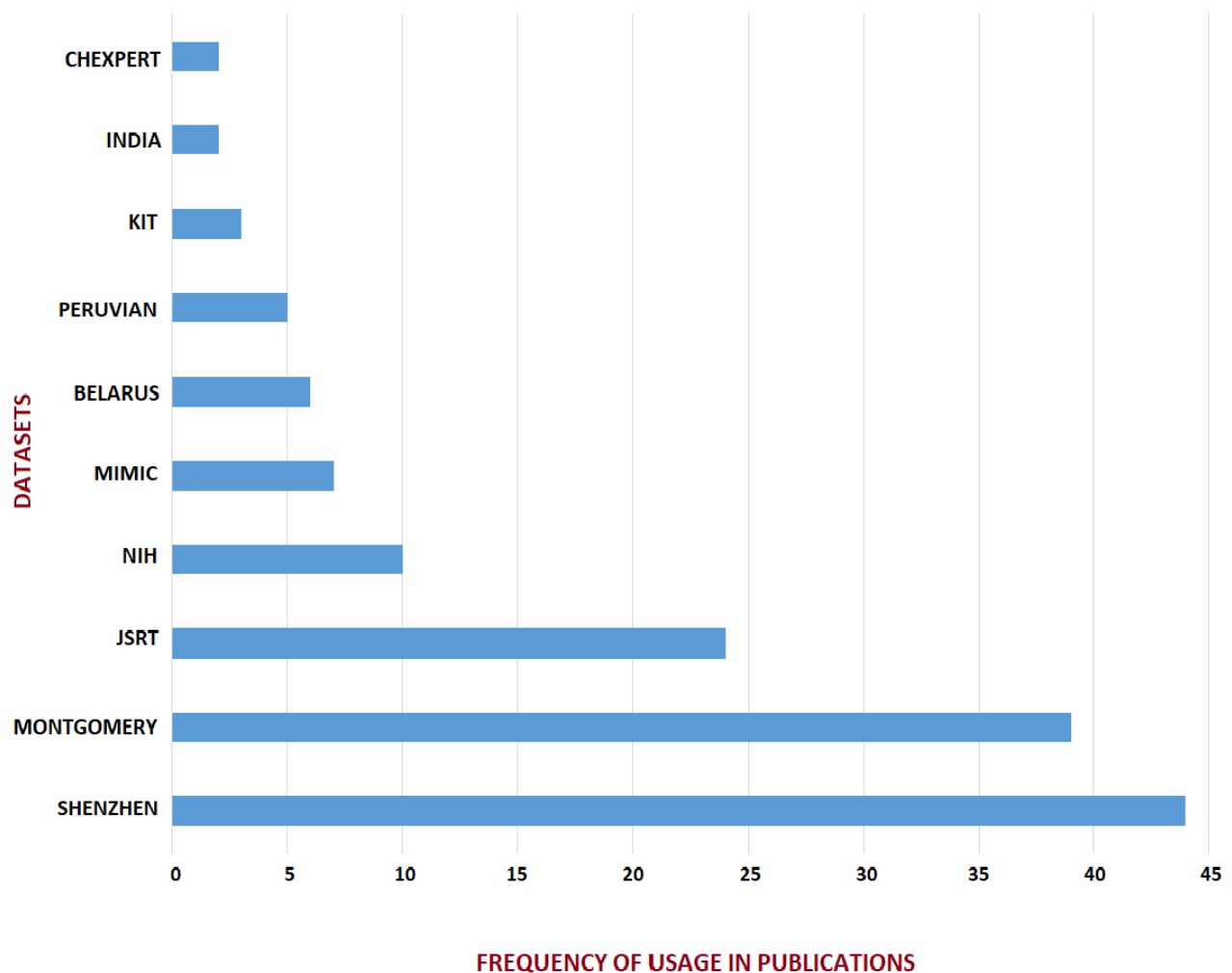


Fig. 10. A bar chart of CXR datasets by frequency of use in publications

that resulted in the development of Point of Care (POC) appropriate for field use [67]. An important aspect that has hugely complicated the quality of diagnosing TB is the desire to differentiate active and latent TB in patients and the negligence of developing on-the-spot screening tools compared to HIV, contributing to diagnosis delays and errors. Various commercial screening products are available for HIV because of the awareness and fear of its deadliness. Meanwhile, TB is ranked more deadly than HIV yet receives less attention concerning on-the-spot commercial screening products.

For effective and timely diagnosis of TB, there is a need to rapidly develop an efficient Point of Care (POC) toolkit

suitable for on-the-spot diagnosis to eliminate diagnostic delays and facilitate rapid treatment for infected patients. It is predicted that the provision of an accurate and broadly acceptable diagnostic POC for TB detection leading to immediate treatment might perhaps prevent about 625,000 deaths yearly arising from the TB epidemic [68].

#### VIII. EVALUATION METRICS

It is important to highlight the various metrics commonly used to evaluate the quality of models and determine how a model is compared with another in terms of performance, strength and weaknesses. The popular evaluation metrics used in the TB detection task are discussed briefly below.

TABLE II  
SUMMARY OF CXR DATASETS

Dataset	Dataset size	Dataset provider
Montgomery County	138	National Library of Medicine, Maryland, USA
Shenzhen	662	National Library of Medicine, Maryland, USA
JSRT	247	Japanese Society of Radiological Technology
Indiana (OpenI)	3996	Indiana University Network for Patient Care
Peruvian	4701	Socios en Salud, Partners In Health in Lima, Peru
KIT	10,848	Korea Institute of Tuberculosis, South Korea
Belarus	304	Belarus Tuberculosis Public Health
India	397	National Institute of Research in Tuberculosis, India
CheXpert	224,316	Stanford Hospital, California
MIMIC	377,110	Beth Israel Deaconess Medical Center (BIDMC), U.S.A
NIH	108,948	National Institutes of Health, Bethesda, MD, USA

#### A. Accuracy

This refers to the rate of the correct outcome from the total number of examined samples [69], [70]. This is given as:

$$Accuracy = \frac{TP + TN}{TP + FP + FN + TN} \quad (1)$$

where

TP: is the case where the model predicts a sample as positive, and it is positive.

TN: is the case where the model predicts a sample as negative, and it is negative.

FP: is the case where the model predicts a sample as positive whereas the actual output is negative.

FN: is the case where the model predicts a sample as negative whereas the actual output is positive.

#### B. Precision

Precision, otherwise known as positive predictive value, is the ratio of positive samples that are accurately predicted [69]. This is given as:

$$Precision = \frac{TP}{TP + FP} \quad (2)$$

#### C. Sensitivity

This is the proportion of the actual positive samples that are correctly identified as positive [71], [72]. This metric is given as:

$$Sensitivity = \frac{TP}{TP + FN} \quad (3)$$

#### D. Specificity

Specificity is the ratio of the actual negative samples that are correctly identified as negative [71], [72]. This metric is given as:

$$Specificity = \frac{TN}{TN + FP} \quad (4)$$

#### E. AUC-ROC Curve

The AUC-ROC, sometimes written as AUROC, is an evaluating metric that indicates the ratio at which a model distinguishes between classes [70]. It tells the probability of separating negative samples from positive samples. Thresholds are set to determine the ROC curve, which is the plot of True Positive Rate (TPR) against False Positive Rate (FPR) given as:

$$TPR = sensitivity = \frac{TP}{TP + FN} \quad (5)$$

$$FPR = 1 - specificity = \frac{FP}{FP + TN} \quad (6)$$

### IX. PRE-PROCESSING

Pre-processing is a vital image processing task that is aimed at transforming raw data into meaningful and efficient data [73], [74], [75] by removing/reducing/correcting unwanted distortions such as noise elimination, missing pixels etc. from the image [12]. In medical image processing, the pre-processing technique is employed to enhance the quality of the image in such a way that the region of interest is clear to reveal the anomaly associated with the raw image for better accomplishment of the subsequent process such as features extraction, segmentation etc. to achieve optimal performance [9]. Image Enhancement, Bone Suppression, and Segmentation are typical approaches for pre-processing CXR images. These approaches are summarised below.

### A. Image Enhancement

It is important to carry out image enhancement to reveal the uncertainty, and low variation associated with CXR images [76]. The process is generally valuable for minimizing diagnosis errors and preserving the image details. Types of image enhancement usually applied to CXR include contrast enhancement, edge features (sharpening, filtering), and noise removal [9], [77], [78]. Contrast enhancement [79], [80] is used to boost the quality of an image by exposing the unclear details associated with it. It ensures the image is suitable for subsequent action, such as feature extraction. An example of contrast enhancement is shown in Figure 11.

Noise removal [77], [81] is applied to reduce or eliminate noise without distorting the image details. Edge features such as image filtering [82] an operation that utilizes the neighbourhood pixel of an image to decide the output value of that pixel, and image sharpening [76] are used to improve the edge of image quality.

### B. Bone Suppression

Bone suppression is an essential pre-processing procedure to ease features extraction, and lung segmentation on CXR [83]. Abnormalities in the lung can be blocked either by the clavicle or ribs, which hinders the feature extraction stage in CAD; as a result of this complexity, it is vital to extricate obstructing bony structures to improve visibility for accurate features extraction [9]. A bone suppression technique is proposed in [84] to suppress the possible overlap between the ribs and lung nodules which makes it difficult to detect abnormalities in the lungs accurately. Another bony structure suppression method was presented in [85] by utilizing k-nearest regression to estimate soft-tissue images such as scapulae and the ribs that overlay the pulmonary region, which ultimately reduces the rate of misclassification. A comparison of the two models was carried out in [86] to identify abnormalities on CXR. One of the models was trained using bone suppression x-ray images, while the other was trained on the original CXR images. The authors found the bone suppression models outperformed the original image model. The utilization of bony suppression method has been proven to improve the performance of pulmonary nodule detection as well as other irregularities like detecting pneumonia [87]. Some additional research work that employed bone suppression techniques includes recognition of lung cancer [88], separation of ribs from other parts of pulmonary images using ICA [89], skeletal bone suppression [90], enhancement of lung nodule [83], and bony thorax decomposition [91] among others.

### C. Segmentation

Sectioning the region of interest is important in processing CXR to extract desired features for specific objectives. The essential task of performing segmentation on images is to group regions with the same pixel value and isolate regions of similarity or a specific part of interest from the original image for further analysis task [12]. Segmentation techniques have been applied to medical images, such as pulmonary nodule detection, abnormalities recognition, lung cancer estimation, pneumonia, detection of TB manifestation, and cardiomegaly. Much research work has been carried out to segment different

regions, but segmenting the lungs is more prominent as a result of its accuracy in delineating fields where specific radiological characteristics show increased density as a result of one or more instances of consolidation, mass, atelectasis, and interstitial [76]. Segmentation techniques can be grouped into Rule-Based, Pixel Based, Deformable, and Hybrid models [9], [92]. These are explained below.

**Rule-based model:** Lung fields are segmented in rule-based models by applying a series of steps and rules for edge detection, region expansion, thresholding, geometrical fitting and many more. The rule-based approach rarely presents a dependable outcome but is a perfect starting point for advanced segmentation techniques [93], [94], [95].

The study in [94], for lung field identification from CXR is based on the first derivative of the vertical and horizontal image profiles to achieve an accuracy of 95.2% and 96.0% respectively for both the left and right lung fields. The author shows that the proposed segmentation algorithm is helpful in detecting lung nodules and rib structure. However, the algorithm was applied to only forty (40) samples and could segment the image one at a time in an average of 0.775 seconds. Hence it will be challenging to determine how the algorithm will perform on large datasets.

An algorithm presented in [95] is based upon thresholding for CXR segmentation. This algorithm sets a threshold for segmenting the image pixels into black, where it is lower than the threshold and white, where it is higher than the set threshold. The procedure in this work was first to determine the left and right lung frame, partition the lung field from the entire image, and further eliminate noise in the image before finally refining the lung edges. Although the author reported an effective result, this was not validated. The study in [93] also utilized a grey-level thresholding approach for lung segmentation and obtained 79% accuracy.

A portable CXR segmentation algorithm that is capable of identifying salient points which are inherently interpolated through Bezier curves was presented in [96]. This algorithm can delineate lung fields smoothly compared to graph cut methods. It can segment portable CXR irrespective of a patient's laying position, which is an issue in some other methods. It also ensures not to exempt the overlapping heart region in detecting lung abnormalities. The efficacy of this model with respect to specificity and sensitivity was measured on only twenty-four CXR samples.

**Pixel-based model:** The pixel model is employed to classify every image pixel into its matching anatomical group, such as diaphragm, heart, and mediastinum [97], [98], [99]. The pixel-based technique is more resilient [100] and has proven to have performed better than the rule-based technique [101].

**Deformable models:** Deformable models are more robust for anatomical boundary segmentation as a result of their flexibility, although impaired by local minima [102], [103]. Examples of deformable models include the Active Appearance Models (AAM) [104], [105], and the Active Shape Models (ASM) [106], [107] briefly discussed below.

Active Shape Model (ASM): introduced in [106] is a statistical model that consistently learns patterns of an object from a given image. Unlike the active contour model, ASM can capture natural irregularities in images of the same category. However, it is time-consuming and expensive because

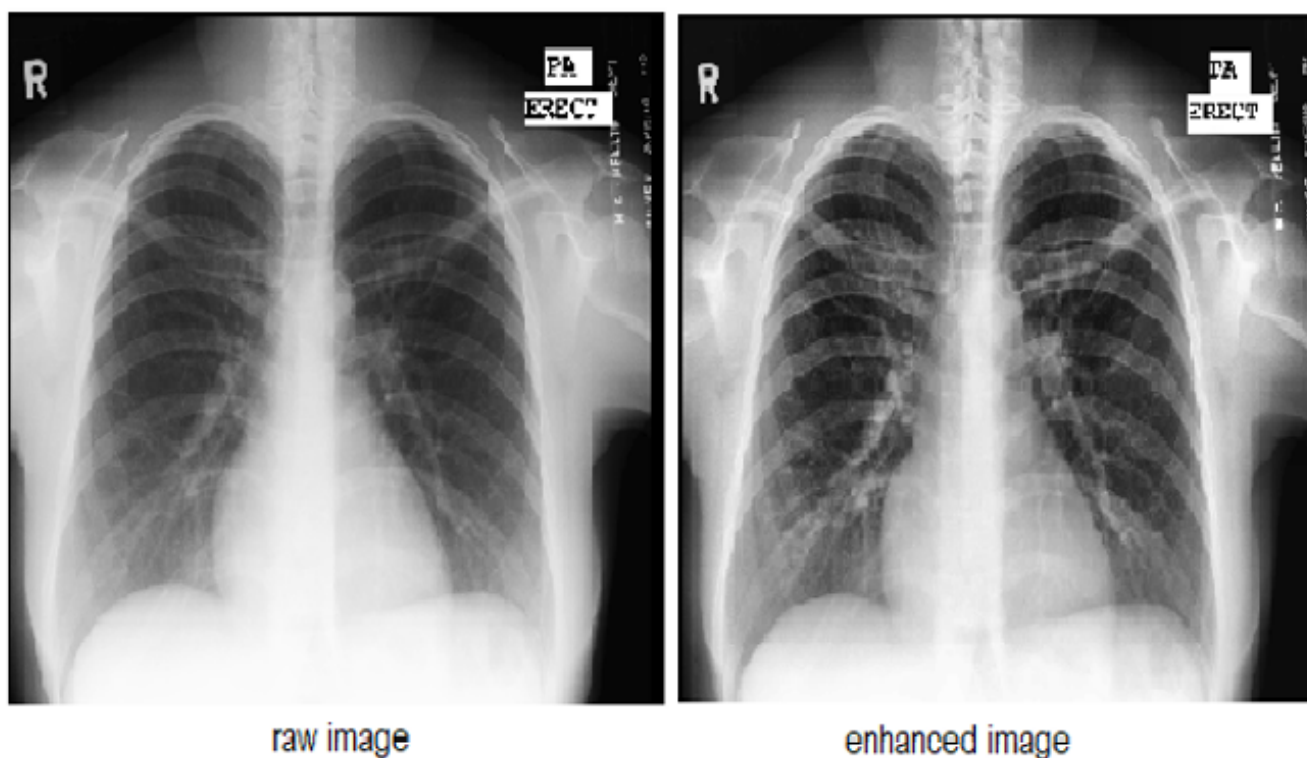


Fig. 11. Samples of the original and enhanced CXR images

it requires multiple landmark samples to represent shape variations. Also, the result of segmentations arising from the ASM application is available to local search fields throughout the landmarks.

In [108], a fusing shape and thresholding framework is presented for lung segmentation by effective integration of shape priors with intensity information which utilized an active shape model for the final fitting. Although the algorithm performed effectively compared to other algorithms, it cannot extract tissues overlapping with the heart. It is also dependent on manual extraction of the lung field by experts.

Active Appearance Model (AAM): [105] is another deformable model that is used widely for image analysis. AAM makes use of the statistical information to learn shape structure from sets of training images [109]. AAM usually consists of a statistical model of the structure and the grey-level appearance of the image that establishes credible examples. A deformable model is presented in [110] for segmentation of lung region in CXR using patients' shape statistics and is population-based. The authors introduced a modified version of the Scale Invariant Feature (SIFT) descriptors to delineate image features around every pixel. The empirical result was reported to proffer a more accurate

and robust segmentation of the lung region. The segmentation model presented in [111] is geared with optimal features that are different to the approach in [106] to find optimal displacement for the landmarks with the use of KNN rather than linear Mahalanobis distance. This model is reported to have achieved a more significant performance than the pioneer active shape model [106] concerning overlap errors.

**Hybrid model:** What is the best segmentation technique for CXR? It is difficult to adequately answer this query since every technique has its essential strengths and weaknesses. To answer this query, one may resort to trying different segmentation techniques and compare their accuracy. The strengths and weaknesses of each technique can be found by comparing them and combining techniques that complement each other to form a hybrid technique. A hybrid segmentation technique is a combination of two or more techniques to take advantage of the strength of each technique and is combined not only to attain a better and more powerful performance accuracy but also to become robust [101].

An automatic algorithm for lung region segmentation was presented in [103] by comparing varieties of segmentation techniques. The authors found that maximum performance was achieved by combining the pixel method with the rule-

based segmentation method, resulting in robust performance accuracy.

A comparison of active appearance model, pixel classification and active shape model, was presented in [101] to segment the lung region, clavicle, and heart in CXR. The three models were applied for lung segmentation, and the pixel-based model showed the highest performance accuracy with no significant difference when evaluated against human observers. Although the human performance was better, the active shape model performed better when applied to clavicle segmentation. As for the heart segmentation, the different models performed worse than the human observer, but the authors concluded that improved performance could be obtained by combining the models with majority voting.

Another hybrid method that used low-level features with prior shape was presented in [112] to solve the local minima challenge arising as a result of strong edge and shading effects due to varying clavicle and rib cage. The hybrid model was optimized and validated upon several images from multiple scanners and various medical sites.

Three mask models were combined in [113] to segment the lung for the detection of TB and other lung abnormalities. After the segmentation task, the study extracted curvatures, texture, and shape features for training a Support Vector Machine (SVM) to classify the CXR images into normal and abnormal classes. According to the authors, the combination of different masks presented a super segmentation of the lung.

An unsupervised model [114] utilized an oriented Gaussian derivatives filter for segmenting a lung on mobile and standard CXR. This model integrated thresholding and fuzzy C-Means for lung field refinement. The model's accuracy, precision, f-score, specificity, and sensitivity were measured on the Japanese Society of Radiological Technology (JSRT) dataset. This is a solely unsupervised model that does not require training to perform lung segmentation.

In [58] a robust nonrigid registration lung segmentation is presented. The model first searches for lung atlases similar to the patient's CXR. It then calculates the patient's definite lung model. Finally, it utilizes the graph cut approach to detect the lung region. The authors reported 95.4%, 94.1%, and 91.7% accuracy for the respective JSRT, MC, and India datasets.

In [115] a method for highlighting the region of interest on CXR for lung segmentation using the K-Means method to analyze the lung features is presented. The patients' physique, gender, and age can be described from the result of the model. Sets of fragmented images were used for their experiments; the image was pre-processed and grouped into 36 x 36, 24 x 24, and 12 x 12 classes to determine the image cluster error. The result reported standing at 28.06%, 30.61%, and 38.49% for the respective clustering errors.

Other conventional segmentation methods include: Gaussian Kernel Fuzzy Clustering [116], Markov Random Field Modeling [117], graph-cut based [118], pattern classification [119], Watershed [120], and Otsu thresholding [121].

#### **Deep Learning-based Segmentations**

Some deep learning-based segmentations are discussed below:

Convolutional Neural Network (CNN) was combined with region proposal for segmentation and object detection pur-

poses in [122]. This hybrid model referred to as a Region-based Convolutional Network, began with accepting input images. The extraction of the region of interest from the image and then employed CNN to compute features for every proposal after the classification of each region was carried out. This model boasted a 62.9% increased mean average precision which is about 50% better compared to the unified framework reported in [123].

An end-to-end segmentation technique for multi-class anatomical structures in CXR using a fully connected neural network was described in [124]. The technique performed better when compared to the human observer for the heart and lung region segmentation. Combining multiple classes ensured the model surpassed modern heart, clavicle and lung field segmentation techniques.

In [125], the study exploited fully a convolutional network to train pixel-to-pixel for semantic segmentation. The model fine-tuned the novel classification approach GoogLeNet [39], [126], VGGNet [127], and AlexNet [34] to the segmentation task and transferred their learned representation into FCNN for the production of a thorough and precise image segmentation to a 20% improvement of PASCAL VOC.

The study in [128] discussed a system that automatically locates and segments nuclei as well as cells in micro images. Structure Correcting Adversarial Network, otherwise known as SCAN, was proposed in [129] for segmenting lung and heart regions in CXR. SCAN integrates a critical network that learns the structures from highest to lowest to differentiate between the ground truth and the synthesized network. The critical network provided an adequate guide to the segmentation network via the adversarial procedures to achieve realistic and accurate results similar to human observers without the intervention of any pre-trained approach.

The deep learning approach presented in [130] is to achieve a fast and accurate lung segmentation that surpasses the complex techniques employed in modern studies. Varieties of the dataset were compared for training their model and illustrated its significance. The authors drew some conclusions: generic, semantic, and segmentation techniques are sufficient enough for the lung segmentation task, thereby emphasizing the fundamental need for a universally dependable lung segmentation tool to further research on severe pulmonary diseases.

A framework for automatic learning of x-ray scans from 3D computer tomography (CT) is proposed in [131] using task-driven based generative adversarial networks. This framework trained a deep image-to-image model for multi-organ segmentation fulfilled from CT volumes, followed by the development of task-driven GANs for obtaining simultaneous synthesis and parsing for invisible X-ray images. The model achieved 89% accuracy as well as a dice average of 86%.

In [132] a model to augment three CNN architectures with organs contour information for segmentation from CXR was proposed. The model was evaluated on the JSRT dataset and reported to perform better than previous models, which utilized the same dataset with respect to segmentation of the lung region, clavicle, and heart.

TABLE II: Existing chest x-ray segmentation methods.

Authors Ref	Database / Size	Assessment Measurement	Result%	Year
[119]	Custom (33)	Accuracy	LDA = above 70%, KNN = above 70%, NN = above 76%	1993
[99]	Custom (198)	Accuracy, Sensitivity, Specificity	Accuracy = 94.8%, Sensitivity = 90.7%, Specificity = 97.2%	1998
[93]	Custom (600)	Accuracy	79%	1998
[97]	Custom (115)	Accuracy	94%	2000
[94]	Custom (40)	Accuracy	Left lung = 95.2%, Right lung = 96.0%,	2001
[111]	Custom (230)	Overlap Score	Left lung =0.887%, Right lung = 0.929%	2002
[110]	JSRT (247)	Average Overlay	ASM Sift = 87%, ASM Intensity = 92%	2008
[96]	Custom (24)	Sensitivity, Specificity	Sensitivity = 94.3%, Specificity = 95.3%	2008
[116]	JSRT (52)	Accuracy	97.8%	2009
[108]	JSRT (247)	Overlap Percentage, Contour Distance in Pixel	92% (22), 94% (28) landmarks, 3.71% , 2.46%	2011
[58]	JSRT, MC, India (585)	Accuracy	JSRT - 95.4% , MC - 94.1% , India - 91.7%	2013
[114]	JSRT (154)	Accuracy, Sensitivity, Specificity, F-score	All above 90%	2015
[125]	PASCAL VOC,NYUDv2,SIFTFlow.	Mean IU	62.2%	2015
[122]	ILSVRC2013 (200)	Mean Average Precision (mAP)	62.4%	2015
[129]	MC, JSRT –	Intersection Over Union	Lungs = 94.7%, Heart = 86.6%	2017
[124]	JSRT	Dice Coefficient, Jaccard Coefficient	Lungs = 97.4%, Colarbone = 92.9%, Heart = 93.7%	2018
[115]	Fragmented Images	Clustering Error	12x12 = 38.49%, 24x24 = 30.61%, 36x36 = 28.06%	2020
[131]	NIH (500)	Dice Average, Accuracy	86%, 89%	2020
[132]	JSRT (247)	Jaccard Overlap Coefficient	Lungs = 0.971% Clavicle = 0.903% Heart = 0.933%	2020

Generally, the challenges of segmenting the lung region have received substantial attention. Diverse approaches have been employed, resulting in good results. Although we can say that lung field segmentation issues have been solved, there is a need to validate the reported results on large datasets to ascertain that various approaches are reliable enough to generate satisfactory results. Table II presents the summary of CXR segmentation.

#### X. AUTOMATIC TB DETECTION TECHNIQUES: FEATURES EXTRACTION AND CLASSIFICATION

Various researchers have employed different approaches to detecting pulmonary TB. More techniques are currently being studied to ensure a real-time diagnosis accuracy for the total eradication of the deadly disease that is most prevalent in developing nations. These approaches and processes are discussed as follows.

A CNN model was used in [133] to diagnose TB from the Montgomery County CXR dataset automatically. The CXR was fed into the model consisting of four convolutional layers and a fully connected layer. The model was configured and trained using Stochastic Gradient Descent at a 0.001 learning rate with an L2 regularizer to control overfitting. The model was trained with 75% of the dataset and tested on the remaining 25% to record an accuracy rate of 87.1%.

The study presented in [134] evaluated the effect of three image enhancement algorithms on the performance of the deep learning method to address the low contrast to improve visualization of CXR. The authors performed enhancement on the Shenzhen dataset and used the image to train EfficientNets and ResNet architectures for transfer learning. The experiments performed to detect TB from the enhanced images achieved 89.92% and 94.8% accuracy. The study concluded that using image enhancement algorithms to pre-process CXR images would thus allow the tested pre-trained network to learn a better model.

A method using wavelets transformation was proposed in [135] for the detection of TB by decomposing CXR scans into low and high-frequency components. The study investigated the CXR of a patient confirmed to have TB, then assigned coordinates and subset the image based on the coordinates assigned to obtain about thirty (30) line profiles, each represented by 26 Daubechies coefficient. Statistical analysis is then performed using SPSS and hierarchical clustering to determine the features for identifying the presence of TB in CXR images.

Transfer learning of nine pre-trained CNN models was employed in [136] to detect TB from CXR and classify it into TB and non-TB. The CXR was first subjected to pre-processing, segmentation and augmentation before classification. Three experiments were carried out: segmentation of CXR using U-net models, then the classification of CXR with and without segmented lung fields. Out of the nine pre-trained models, ChexNet performed better to obtain an overall accuracy of 96.47% for the classification without segmentation. In contrast, DensNet201 obtained the best result in the category with segmentation. The study further employed visualization techniques to confirm that CNN learns dominantly from the segmented lung regions, resulting in higher detection accuracy. The study showed that the effect of performing image pre-processing and segmentation

of lung fields could improve classification accuracy. The evaluation metrics examined in the study were accuracy, F1-score, precision, sensitivity, and specificity.

An experiment was done in [137] to compare the performance of three different methods in detecting TB in the lungs. The obtained results from the experiment showed the K-Nearest Neighbor (KNN) classifier had a maximum accuracy of 80%, Simple linear regression 79% accuracy, and the Sequential minimal optimizer obtained 75% accuracy. The approach presented in [9] for TB detection began by employing a graph-cut approach to segment the lung fields, then computed shape features and textures using the binary classifier (BC) and SVM to classify the CXR images into healthy and unhealthy classes. The method boasted 78.3% and 84% accuracy for both datasets.

Early detection of TB is presented in [138]. The homomorphic filter, median filter, and histogram equalizers were first applied to pre-process the input image. The pre-process image was then segmented using the active contour and finally obtained the classification output using the mean values. Although there was no accurate result reported in the study, the authors affirmed the impact and contribution of CAD as an assistive tool to guide radiologists and doctors in reaching an accurate and timely diagnosis decision concerning TB detection.

In [139], the authors present a TB identification system using a bright field microscope. The study further compared pixel, SVM, KNN, Linear Regression, Quadratic Discriminant, and Probabilistic Neural Networks classifiers which produced a result above 95% for the accuracy, sensitivity and specificity. The use of this system for TB screening may reduce the involvement of a technician, according to the authors.

A comprehensive study that combined geometrical and advanced textural features for the detection of TB cavity is presented in [63]. The study first extracted cavity field from CXR scans with the use of histogram of oriented gradients, local binary pattern, and Gaussian model template matching at the coarse-scale, then applied active contour snake-based and eigenvalues of the Hessian matrix to enhance the extracted field and lastly, utilized SVM classification to reduce false positives on a fine scale with gradient inverse coefficient of variation, Kullback-Leibler divergence, and circularity measure. The rate of true cavity achieved in the experiment is reported to perform better than existing methods.

In an attempt to limit the time taken by radiologists to examine patient CXR scans, [140] employed texture features to identify and classify thoracic x-ray scans as infected and non-infected. Several statistical features of the x-ray histogram were calculated and reduced with principal component analysis and then finally classified the image using a minimum distance classifier. The result of 95.7% accuracy was presented.

[141] employed CNN architecture to detect TB from the Shenzhen CXR dataset. The study began with pre-processing the CXR before propagating it through the CNN models composed of 6 convolutional layers with two fully connected layers. 70% of the dataset was utilized for model training while 30% was used to evaluate the model, which achieved 87.8% accuracy. Data augmentation and some hyper-parameters employed in the study helped control

model overfitting.

In [142] granulometry and correlation technique was utilized to detect the miliary TB region. Template matching and correlation were performed by transforming the template and the image into a frequency domain. The authors strived to minimize false positives and negatives in the training set by correlating every image with 16 templates of varying sizes and respective thresholds. The technique achieved a 94% accuracy.

In [143] a hybrid of several methods, including edge detection, rib image processing, boundary tracing and information extracting methods, was used to establish a localized frame of reference in CXR. Binarization of the CXR was done for ease and quick extraction of the rib line, followed by implementing other algorithms such as seed growth and morphological openings to achieve about 85% accuracy for the automatic detection of focal opacities.

The method presented in [113] is aimed at TB diagnosis from Posteroanterior CXR. The system combined a log Gabor mask, statistical lung model mask, and intensity mask to segment the lung region, followed by curvatures, textures, and shape features. These extracted features were then utilized in training an SVM classifier to differentiate the healthy images from the infected images. The system performed at 75% accuracy and about 83.12% AUC.

CXR interpretation using a statistical approach for identifying lung TB is proposed in [14]. Wavelet transformation was first applied to each x-ray image region of interest to convert the image into four labelled subsets representing the vertical, diagonal, trend, and horizontal coefficients. The following procedure was to apply principal component analysis on 12 measures to minimize dimensionality and finally use discriminant functions with probability ellipsoids to determine the misclassified probabilities. The system achieved a 94% classification accuracy.

A computer-aided detection system is presented in [144] based on multi-varied dissimilarities. The method estimated global dissimilarities classified by adopting a linear discriminant classifier to codify the CXR image into normal and suspected TB classes. The result of the global dissimilarity classification reached 0.81% AUC compared to 0.83% when combined with the local classification.

The algorithm proposed in [145] is aimed at enhancing CXR images to remove noise by segmenting the lung field and applying contrast enhancement that makes it easier to extract features associated with the identification of TB manifestations. There was no report of the system performance and validation accuracy. Hence, the reliability of the system could not be ascertained.

The CNN structure employed in [37] consists of seven convolutional layers and three fully connected layers to perform classification experiments on CXR for diagnosing TB. The authors compared three variety optimizers in their experiments and found the Adam optimizer performed better with a validation accuracy of 82% and loss of 0.40%. The result of their experiment was validated on the Shenzhen and Montgomery datasets.

The research presented in [56] was one of the first to employ deep learning techniques on medical images. The work was based on famous AlexNet architecture and transferred learning to screen system performance on different datasets.

The cross-dataset performance analysis shows the system's accuracy of 78.3% and 86.9% on the Montgomery dataset with 84.1% accuracy and AUC of 0.90% on the Shenzhen dataset.

The study carried out in [36] presented proposals to improve feature extractors in detecting diseases using pre-trained CNN. This research is famous for combining multiple instance learning algorithms with pre-trained CNN, assessing classifiers trained on extracted features, and comparing existing models' performance analysis for extracting features from the CXR dataset. The experimental result for the Montgomery dataset, GoogLeNet, achieved the highest accuracy, while the best results for the Shenzhen dataset were obtained with the ResNet model.

An experiment for TB screening was presented in [38] using AlexNet and VGGNet architectures for the classification of CXR into positive and negative classes. The analysis carried out on the Montgomery and Shenzhen CXR datasets showed that VGGNet outperformed Alexnet due to a deeper network of VGGNet. The performance accuracy of 80.4% was obtained for Alexnet, while VGGNet reached 81.6% accuracy. The authors concluded that improved performance accuracy was possible by increasing the dataset size used for the experiment.

In [146], a framework is made up of a set of segments that must be executed in sequence to detect TB manifestation in CXR. The procedure begins with pre-processing based on the Pyramid Histogram of Oriented Gradients (PHOG) and Generalized search tree (GiST) descriptor, then selects features based on chi-square and then utilizes the SVM classifier to build the model to obtain the result. The authors further developed a toolkit in Matlab for training and predicting new CXR images.

In [147], a method is described to segment the lung region on CXR based on Watershed. They incorporated some assumptions that the background area and the lung were greater than 30% and 20% of the image frame. A fixed-sized window scan found the maximum grey levels and the average of the image pixels. It then employed an intensity threshold to classify the window midpoint as a suspected nodule.

A deep CNN is presented in [40] for pulmonary TB classification as either healthy or unhealthy. The images were classified using GoogLeNet and AlexNet architectures after applying pre-processing technique and performing an ensemble on the image. The authors also employed the services of a professional radiologist to interpret the images in cases where both classifiers differed. AUC, specificity and sensitivity were used as metrics to measure the mode.

A CNN model that involved classifications of different manifestations of TB was presented in [41]. This work looked at unbalanced and less categorized CXR scans and incorporated cross-validation with sample shuffling in training their model. It was reported to have obtained 85.6% accuracy in classifying the various manifestations of TB using the Peruvian dataset.

CheXNeXt is an algorithm developed by the authors in [148] for the identification of 14 various pathologies in CXR. The algorithm employed the CNN approach was validated on the NIH dataset and compared the result with the interpretations of 9 professional radiologists. The result

showed that CheXNeXt achieved an equivalent performance with the radiologists in 10 different pathologies, with the best performance in 1 pathology and underperformed in 3 pathologies. The algorithm took less than 2 minutes to identify the various pathologies, while the radiologists took 240 minutes.

Another study that employed CNN in detecting various pathologies in CXR is presented in [149]. The study fused GiST and CNN descriptors and was evaluated on a non-medical image dataset to obtain the system AUC, and the sensitivity and specificity were between 0.87% - 0.94%.

The authors in [150] present an algorithm to assess the efficacy of deep learning architecture for abnormalities detection in CXR. NIH CXR 8 dataset [61] was used to train their algorithm that was based on CNN to identify specific CXR abnormalities such as infiltration, nodules, pneumonia, effusion, etc. to ascertain the standard of reference for the study. The service of a professional radiologist was employed to assess the presence of abnormalities in the CXR. The data analysis was done using SPSS and Excel. The experiment results show AUC ranged between 0.693-0.923% for the radiologist's interpretation and 0.837-0.929% for the deep learning approach for all abnormalities. The study further concluded that although the use of deep learning was important in interpreting accuracy and could improve the level of detection of abnormalities, it was unlikely to replace the input of a radiologist entirely.

In [64], an automatic deep learning algorithm for diagnosis of active lung TB aimed at streamlining the process of screening and detection was presented. The algorithm was developed using CNN, comprising about 27 layers. The CXR images were resized, and then a geometric and photometric operation was applied to them before passing them on to the CNN architecture for training. The algorithm was evaluated on two public datasets and four custom datasets and compared with the interpretation of a certified radiologist and physicians. The algorithm's performance showed significantly higher classification accuracy than the radiologist and physicians' performance on all the datasets.

Deep learning was also employed in [151] for the detection of TB manifestation on CXR. Their CNN approach incorporates demographic information to train images containing 1000 normal and infected samples, using five different CNNs architectures as feature extractors. The experimental result in comparing the output of DCNN to I-CNN shows DCNN performed better. In general, the authors demonstrated that incorporating demographic information such as gender, age, weight, and height of the patients with the CNN model resulted in an improved and effective diagnosis of TB.

A model that is composed of data acquisition and recognition stage for the detection of TB is presented in [152]. The images used in this model consisted of a field of view digital images acquired from a microscope. The images were fed into the recognition stages that used a transfer learning model which learns from fine-tuned pre-trained weights. SVM was then employed to classify the images into infected and non-infected classes. The model attained a 95.05% accuracy.

The work presented in [70] aimed to detect about 20 abnormalities from CXR. The study employed three different public datasets and found that a hybrid ensemble model with Deep Convolutional Neural Network (DCNN) outperformed

utilizing the DCNN alone, which did not show better performance across the various abnormalities reported in the study. The result of their ensemble model showed more significant improvement when compared to the AlexNet, VGG-16, 19, ResNet-50, 101 and 152 in terms of accuracy, specificity, sensitivity and AUC.

In [153], a study that employed pre-trained CNN (GoogLeNet) was presented to automatically identify and classify CXR images as either normal, which means healthy, or abnormal with the presence of one or more instances of pleural effusion, consolidation, pneumothorax, cardiomegaly, and pulmonary edema. Area Under the Curve (AUC) was the metric used to measure the model's performance in interpreting a board-certified radiologist. The results obtained were 0.964% AUC, 91% sensitivity and specificity for the healthy classes, while different percentages were obtained for the various abnormalities classes.

In [154], the authors participated in the 2019 ImageCLEF challenge and presented a Deep Learner model (LungNet) that focused on automatic analysis of TB from computer tomography CT scans. The CT scans were first decompressed, and the slices were extracted with 512 images for the X and Y dimensions and between 40-250 images for the Z dimension. Filters were then introduced to eliminate the slices that did not contain valuable information required for classifying the samples. The proposed LungNet and ResNet-50 architecture were employed as the Deep Learner, whose outputs are the preliminary results. The Deep Learner model was trained on 70% and 50% training sets and achieved AUC performance of 63% and 65% for the ImageCLEF CT report and severity scoring task. Although these performances were not the best presented in the challenge, the authors believed if they were subjected to advanced pre-processing techniques such as data augmentation and masking, these could provide better performance.

A model proposed in [155] employed a learning concept to transfer the knowledge acquired from training a model as a starting point for the new model. The deep CNN model pre-trained on the ImageNet dataset was adopted as a features extractor on the CXR rather than an end-to-end network. The extracted features were used to train a classifier to obtain the final classifications of the images. The model achieved 95.80% classification accuracy and precision of 96%. The study shows that transfer learning helped overcome the challenges of the limited dataset.

The study in [156] was conducted to assess the detection accuracy of qXR, which is a computer-aided diagnosis software based on CNN. The authors utilized microbiologically established lung TB images as the standard for reference and used the kappa coefficient and confidence interval as the statistical tools to analyze the data and examine the inter-rater reliability of radiologists in detecting specific lung abnormalities. The study also used radiologist interpretation as a standard to validate the detection accuracy of the qXR in terms of generation ROC curves and to calculate AUC. The qXR system achieved 0.81% AUC for the detection of lung TB, with 71% sensitivity and 80% specificity.

The development of a deep learning model is presented in [157] for identifying abnormalities in CXR scans. The model was trained using large datasets up to about 2 million images using CNN. The model development began with down-

sampling, resizing, normalizing and augmenting the CXR before feeding them into the training network for features extractions and classification, after which validation was performed to compute accuracy metrics. The model attained an AUC of 0.92 for the general abnormalities detection and 0.96 for specific manifestations. The study confirmed that having extensive data to train a deep learning model will obtain a higher detection rate.

The study presented in [62] evaluates and compares a commercial software CAD4TB for detecting TB manifestation on CXR. The software has different versions ranging from versions 3, 4, 5, and 6. Each version uses different classifiers like SVM, KNN, and DCNN and is composed of features that are not common to all versions, such as symmetry check, shape analysis, a heat map and texture analysis.

The CAD4TB version 6 is said to outperform other versions obtaining 76% specificity and 90% sensitivity, while comparing version 6 to standard radiological inference attained a higher performance of 98% specificity and 90% sensitivity.

The study presented in [158] employed a Bayesian Convolutional Neural Network (BCNN) for identifying uncertainty with low perceptibility associated with normal and abnormal TB manifestation on CXR. The fusion of Bayesian with CNN aimed to overcome the limitation of the Softmax classifier in CNN models. The BCNN model was evaluated on both Shenzhen and Montgomery datasets to obtain 86.46% and 96.42% identification accuracy.

Three pre-trained CNN models were employed in [159] to detect and classify TB from CXR. Each model was fine-tuned and trained separately on the Shenzhen dataset and evaluated with the Montgomery set. The results of these models were averaged through bagging to build an Ensemble classifier. The Ensemble model takes advantage of the strengths of different pre-trained CNN models such that a misclassification from one model can be detected and corrected by other models.

The study in [160] proposed an Ensemble of five state-of-the-art models toward learning modality-specific features from different CXR datasets. The knowledge learned through modality-specific is transferred and fine-tuned for TB detection tasks on the Shenzhen CXR dataset. The predictions of the best performing models are combined using different ensemble methods to demonstrate improved performance over any individual model in classifying the CXR as infected or healthy. The evaluation of the proposed model achieved 99.0% AUC with 94.1% accuracy.

Another study that employed Ensemble models is presented in [161]. Distinctive features were extracted from edge detected images and raw CXR images for TB detection. Before developing different classifiers to represent Ensemble, image pre-processing was applied to both image categories. The model's performance was evaluated, and the Ensemble model outperformed the individual models at 89.77% accuracy and 90.91% sensitivity.

A hybrid model (MobleNet-AEO) was proposed in [162] to classify CXR images as TB and Not-TB. The proposed model first employed MobileNet as feature extraction and then used the Artificial Ecosystem-Based Optimization (AEO) as the feature selector. The model was trained with the Shenzhen and a private dataset to achieve 90.2% and

94.1% accuracy.

A model that combines transfer learning with CNN is presented in [163] to develop a system to detect and classify TB culture tests. The model was trained using small and imbalanced data samples obtained from the Tao-Yuan General Hospital in Taiwan. The study employed SMOTE to resolve the imbalance and introduced a two-stage classification method to improve recall of non-negative, which eventually reached 98% recall. The preliminary result of this approach showed a promising output.

Deep CNN models proposed in [164] were integrated with the handcrafted technique through Ensemble learning as a feature extractor from CXR. The extracted features were then used as inputs to train a classifier to detect infected CXRs. The model was evaluated to compare the performance of both methods, and the Ensemble model performed better at 0.99% AUC.

A lightweight EfficientNets model that achieved state-of-the-art results on ImageNet was fine-tuned on the CXR images and implemented for the classification of TB in [165]. The model scaled down the number of parameters using a global average pooling to control overfitting and incorporated robust image pre-processing techniques that enhanced the visibility of the images and generated replica samples of the original datasets to increase and improve the performance of models. The results obtained with the fine-tuned EfficientNets B0 – B4 were averaged to build an ensemble classifier.

A summary of automatic TB approaches is presented in Table III while Figure 12 presents the analysis of the techniques using a bar chart to show the most prominent classifiers used in CAD development for TB detection.

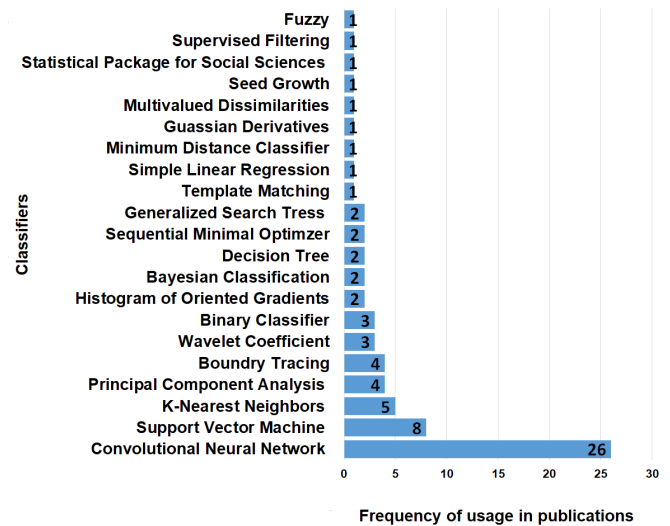


Fig. 12. Bar chart showing classifiers used for TB detection.

TABLE III: Automatic TB detection. Enumerating the methods, datasets, evaluation metrics, performance, manifestations, and year of publications

Authors Ref	Methods	Datasets	Assessment	Result%	TB Manifestation	Year
[137]	Sequential minimal optimizer, linear regression, K-nearest neighbor	Shenzhen	Efficiency	75%, 79%, 80%	All	2017
[9]	Support vector machine, Binary classifier	Montgomery Country and Shenzhen	Accuracy	78.3%, 84%	All	2013
[133]	Convolutional neural network	Montgomery Country	Accuracy	87.1%	All	2020
[142]	Granulometry, Template matching, Fourier domain correlation, Threshold, Rolling ball algorithm	Custom: Obtained at Groote Schuur Hospital. Cape Town, South Africa	Accuracy	94%	Miliary	2001
[139]	Bright-field microscope	Custom: Data were captured using a Nikon Microphot-FX microscope	Accuracy, Sensitivity, Specificity	Above 95%	All	2009
[141]	Convolutional neural network	Shenzhen	Accuracy	87.8%	All	2020
[63]	Histogram of oriented gradients, Gaussian model template matching, Local binary pattern, Support vector machine, Kullback-Leibler divergence, Circularity measure, Gradient inverse coefficient of variation	Custom: CXR collected from the University of Alberta Hospital	Accuracy	82.8%	Cavity	2013
[140]	Textural features, Principal component analysis, Minimum distance classifier	Custom: CXR collected from Sarjito Hospital Yogyakarta	Accuracy, Fault acceptance rate, Fault rejection rate	95.7%, 3.33%, 6.67%	All	2013
[166]	Decision tree, Texture features, User-guided snake algorithm	Custom: Obtained from SATA CommHealth Singapore	Accuracy, Precision, Specificity, Sensitivity, AUC	94.9% 92.9% 95.4% 92.8% 91%	All	2012

*Continued on next page*

TABLE III – Continued from previous page

Authors Ref	Methods	Datasets	Assessment	Result %	TB Manifestation	Year
[167]	Bayesian classification, Gradient inverse coefficient of variation, Circularity measures	Custom	False positive, Accuracy	0.237%, 82.35%	Cavities	2010
[143]	Edge detection, Boundary tracing, Seed growth, Morphological openings	Custom	Accuracy	85%	Focal opacities	2010
[113]	Log Gabor mask, Intensity mask, Lung model mask, Support vector machine	Montgomery Country and, Japanese Society of Radiological Technology	Accuracy, AUC	75% 83.12%	All	2012
[14]	Wavelet coefficients, Maximum column energy, Principal component analysis	Institute of Respiratory medicine Malaysia	Accuracy	94%	All	2010
[144]	Gaussian derivatives, Multivalued dissimilarities, Voting rule, Central moments	Custom: Obtained from Delft imaging system Netherlands	AUC	0.81% 0.83%	All	2009
[155]	Pre-trained convolutional neural network	Montgomery Country and Shenzhen	Accuracy, Precision	95.8%, 96%	All	2010
[37]	Convolutional neural network	Montgomery Country and Shenzhen	Overall accuracy, Validation accuracy	97.4%, 82.9%	All	2017
[56]	Convolutional neural network, transfer learning	Montgomery Country, Korea Institute of TB, and Shenzhen	AUC, Accuracy	86.9%, 90% 78.3%, 84.1%	All	2016
[36]	CNN feature extractor, Bag of features, Ensembles, SVM	Montgomery Country, Shenzhen, and National Institute of TB and Respiratory Diseases. New Delhi	Accuracy, AUC	0.782%, 0.834% 0.838%, 0.912%	All	2017
[38]	Pre-trained CNN	Montgomery Country and Shenzhen	Accuracy	80.4%, 81.6%	All	2017
[146]	Wavelet denoising, Pyramid histogram of oriented gradients, Chi square, Gist, Support vector machine	DA and DB: National Institute of TB and Respiratory Diseases New Delhi, India	Accuracy	0.94%, 0.92%	All	2014

Continued on next page

TABLE III – Continued from previous page

Authors Ref	Methods	Datasets	Assessment	Result %	TB Manifestation	Year
[40]	Deep convolutional neural network, Ensemble	De-identified Health Insurance Portability and Acountability Act (HIPAA)	AUC, Sensitivity, Specificity	0.99%, 97.3%, 100%	All	2017
[41]	Convolutional neural network	Peruvian partners at socios en salud (Peru)	Accuracy	85.6%	All	2017
[148]	Convolutional neural network	NIH CXR-14	AUC	0.831%, 0.704%, 0.851%, 0.808%	All	2018
[149]	Pre-trained Convolutional neural network, Support vector mahine, Principal component analysis, Generalized search tree	Custom: Non-medical diagnostic image obtained from department of Sheba medical centre, Tel-Hashomer, Israel	AUC, Sensitivity, Specificity	0.87% to 0.94%	Pleural Effusion, Cardiomegal, Mediastinum	2015
[150]	Convolutional neural network, Statistical Package for the Social Sciences (SPSS)	NIH CXR-8	AUC	0.693 to 0.923%, 0.837 to 0.929%	Pleural effusion, Hilar prominenc, Pulmonary opacity, Enlarged cardiac silhouette	2018
[64]	Convolutional neural network	Seoul national University Hospital, Boramae Medical Center; Kyunghee University Hospital at Gangdong, Daejeon Eulji Medical Centre, Montgomery Country, and Shenzhen	AUC, Sensitivity, Specificity	0.977, 0.973%, 94%, 91.1%	All	2019
[70]	Ensemble, Deep Convolutional neural network	Japanese Society of Radiological Technology, Shenzhen, and Indiana	Accuracy, Sensitivity, Specificity, AUC	90%, 96%, 96%, 0.94%	All	2017
[153]	Convolutional neural network	Custom	AUC, Sensitivity, Specificity	0.964%, 91%, 91%	All	2017

Continued on next page

TABLE III – Continued from previous page

Authors Ref	Methods	Datasets	Assessment	Result %	TB Manifestation	Year
[151]	Convolutional neural network, Deep convolutional neural network	Custom	AUC, Sensitivity, Specificity	0.9075%, 0.815%, 0.962%	All	2019
[152]	Transfer learning, Support vector machine	Digital images acquired from a microscope	Accuracy	95.05%	All	2019
[154]	Convolutional neural network, Supervised and unsupervised filtering, Support vector machine	CT scans of TB patients	Accuracy, AUC	0.60% 65%, 63%	All	2019
[156]	Convolutional neural network, Kappa coefficient, Confidence Interval, Youda index	CXR of patients at Kasturba hospital Manipal, India	AUC, Sensitivity, Specificity	0.81% 71%, 80%	All	2020
[157]	Convolutional neural network	Custom: Collected from 45 hospitals around the world	AUC,	0.96%	All	2020
[62]	Convolutional neural network, Support vector machine, k-nearest neighbors	Custom: Acquired from Sehatmand Zindagi healthy life centre Karachi, Pakistan	Specificity, Sensitivity	76%, 98%, 90%	All	2020
[160]	Ensemble of deep convolutional neural network	Shenzhen, RSNA, Indiana	Accuracy, AUC, Specificity, Sensitivity	94.1%, 99.0%, 100%, 92.6%	All	2020
[161]	Ensemble of two deep convolutional neural network	Shenzhen and Montgomery County	Accuracy, Sensitivity, Specificity	89.77%, 90.91%, 88.64%	All	2019
[162]	MobileNet, Artificial ecosystem-based optimization	Shenzhen	Accuracy	94.1%	All	2020
[159]	Deep convolutional neural network	Montgomery Country, and Shenzhen	Accuracy, Sensitivity, Specificity	96.14%, 90.03%, 92.41%	All	2021
[164]	Deep convolutional neural network	Montgomery Country, and Shenzhen	AUC	99.0%,	All	2021
[165]	Efficientnets	Montgomery Country, and Shenzhen	Accuracy, Sensitivity, Specificity, AUC	97.44%, 99.18%, 96.21%, 0.94%	All	2021

## XI. DISCUSSION

In this study, we have presented both the conventional methods and state-of-the-art approaches to diagnosing TB. Automatic detection of TB has received tremendous attention over the years, with diverse research papers being published concerning abnormalities detections in CXR. It is challenging to judiciously compare and contrast the performances of the various algorithms employed to identify TB manifestations due to different datasets that may have been collected under different conditions with other devices and the severity of abnormalities. Some datasets are accompanied by a radiological interpretation that serves as a ground-truth to assist researchers in justifying their findings. These algorithms have assisted medical experts, and professional radiologists in substantiating their diagnosis opinions and providing quicker/faster screening of the patients CXR to shed excessive workloads.

It is shown from the literature that the use of deep learning algorithms [56], [70], [153], [165] has performed more accurately in classification tasks such as TB detection compared to other automatic methods like SVM, KNN, ANN, and Bayesian classifier. Also, earlier methods can only detect one or a few diseases simultaneously. In contrast, deep learning algorithms can detect many diseases at the same time directly from CXR, which agrees with the interpretation of a skilled radiologist. Despite the varieties of potentials offered by deep learning algorithms for classifying images, there are still some challenges like the inability of the Softmax layer to detect uncertainties in classification and the unbalanced distribution of samples with respect to limited datasets. Since it involves extracting distinct features from images, having limited datasets could often result in poor network generalization. Therefore, there is a need to test a large number of data samples collected from different regions and captured with different devices under different atmospheres to ensure versatility and better model generalization.

The implementation of deep learning algorithms in training big data has resulted in considerable progress. However, it is time-consuming due to feature extraction, which progresses from the shallow stage to a deeper level via convolutions. Machine learning algorithms like KNN, SVM, etc., also have the potential for improvement and should be considered to attain high-performance accuracy. Most of the algorithms have reported tremendous results in literature but are not transformed into CAD tools to be used in real-life scenarios. Also, the systems should be evaluated against independent observers to assess if they can attain the same level as human performance or surpass expert radiologists at some point. deep learning methods also require extensive hyper-parameter tuning to train the model. Resizing the input image to a much lower resolution may result in the loss of some essential diagnostic features and could limit performance.

## XII. CONCLUSION AND FUTURE DIRECTIONS

A comprehensive survey of automatic methods for the diagnosis of pulmonary TB from CXR is presented in this paper. The emphasis is on the CAD systems involving image pre-processing, feature extractions, and feature classifications. Image enhancement and segmentation are fundamental

procedures in image pre-processing to boost the quality of images, making them clearer to extract distinct features in order to attain quality classifications. All these techniques are discussed and summarized in Table II and Table III. It is evident that the deep learning models discussed in this work have performed excellently in image classification tasks over the traditional machine learning approaches like SVM, ANN and the like. deep learning models have become mainstream these days and promise more potential for image classification tasks, specifically in medical imaging, to detect various abnormalities to support radiological examinations.

From all the models reviewed in this study, we can conclude that state-of-the-art efficientNets have efficiently outperformed other models. EfficientNets are smaller with fewer parameters, faster, and generalize well to obtain higher accuracy on other datasets popular for the transfer learning task. Therefore, the Implementation of efficientNets is recommended for developing sophisticated systems to diagnose pulmonary abnormalities.

This study recommends future research directions that may bring about additional improvement in medical imaging analysis, specifically for TB and other lung diseases. Some of these are:

- Development of algorithms that could distinctly identify foreign objects like rings, buttons, pieces of bone, and coins that may be found on CXR images. These foreign objects could lead to misclassification and impede the performance of detection systems. For instance, round objects like buttons, bone pieces or rings can be mistaken for nodules.
- The abilities of CAD systems to simultaneously detect different diseases.
- A more profound network architecture with sufficient and evenly distributed training CXR images should be investigated in future works.
- Some diseases usually exhibit similar manifestations on the CXR, and this could be a problem leading to misdiagnosis. Several studies are encouraged to differentiate these diseases regardless of their common manifestations adequately.
- A hybrid of traditional machine learning and deep learning models could complement each other in terms of strengths and weaknesses to develop a powerful CAD system.
- Studies incorporating other information such as patients' level of cough and body temperatures to the CAD system could impact general performance accuracy.

The comparative investigation of different models helps in having a better understanding of a project and its implementation. Hence, this study serves as a guide in selecting the right method and techniques more suitable for early TB detection, which could help avert millions of deaths. It is our belief that this extensive review will proffer a better perception of TB detection domain while providing insights for future research.

## XIII. ABBREVIATIONS

CAD: Computer-Aided Diagnosis; CNN: Convolutional Neural Network; TB: Tuberculosis; PCA: Principal Component Analysis; SVM: Support Vector Machine; AUC: Area

Under Curve; ROC: Receiver Operating Characteristic; KNN: K-Nearest Neighbour; ANN: Artificial Neural Network; TP: True Positive; FP: False Positive, TN: True Negative; FN: False Negative; CT: Computed Tomography; DCNN: Deep Convolutional Neural Network; BCNN Bayesian Convolutional Neural Network; PHOG: Pyramid Histogram of Oriented Gradients; VGGNET: Visual Geometry Group Network; Xception: Extreme Inception; CXR: Chest X-Ray; TI: Tuberculosis Index; POC: Point of Care; ILSVRC: ImageNet Large Scale Visual Recognition Competition; WHO: World Health Organizations, JSRT: Japanese Society of Radiological Technology; SPSS: Statistical Package for the Social Sciences; KIT: Korea Institute of Tuberculosis.

## REFERENCES

- [1] W. H. Organization, *Global Status Report on Alcohol and Health 2018*. World Health Organization, 2019.
- [2] M. Levin, M. Kafarou, and L. Coin, "Method of detecting active tuberculosis using minimal gene signature," Oct. 24 2019, uS Patent App. 16/326,828.
- [3] N. A. Knechel, "Tuberculosis: Pathophysiology, clinical features, and diagnosis," *Critical Care Nurse*, vol. 29, no. 2, pp. 34–43, 2009.
- [4] M. G. Ametembun, "Iddf2019-abs-0238 follow-up of small bowel and dry type peritoneal tuberculosis treatment," pp. A107–A107, 2019.
- [5] K. Potts, M. Ragland, A. Hans, and M. Kearns, "Empyema necessitans caused by mycobacterium tuberculosis," in *D58. Pleural Infection Clinical Case and Studies*. American Thoracic Society, 2019, pp. A6842–A6842.
- [6] A. T. Brennan, M. Maskew, B. A. Larson, I. Tsikhutsu, M. Bii, L. Vezi, M. P. Fox, W. D. Venter, P. Ehrenkranz, and S. Rosen, "Who is seeking antiretroviral treatment for hiv now? characteristics of patients presenting in kenya and south africa in 2017-2018," *Journal of the International AIDS Society*, vol. 22, no. 9, p. e25358, 2019.
- [7] W. H. Organization, *Global Tuberculosis Report 2017*. World Health Organization, 2017. [Online]. Available: [https://www.who.int/tb/publications/global\\_report/gtbr2017\\_main\\_text.pdf](https://www.who.int/tb/publications/global_report/gtbr2017_main_text.pdf)
- [8] N. Nair, F. Wares, and S. Sahu, "Tuberculosis in the who south-east asia region," pp. 164–164, 2010.
- [9] S. Jaeger, A. Karagyris, S. Candemir, J. Siegelman, L. Folio, S. Antani, and G. Thoma, "Automatic screening for tuberculosis in chest radiographs: A survey," *Quantitative Imaging in Medicine and Surgery*, vol. 3, no. 2, p. 89, 2013.
- [10] I. Livieris, T. Kotsilieris, I. Anagnostopoulos, and V. Tampakas, "Dtco: An ensemble ssl algorithm for x-rays classification," *Advances in Experimental Medicine and Biology; Springer: Berlin/Heidelberg, Germany*, 2018.
- [11] C. Lange and T. Mori, "Advances in the diagnosis of tuberculosis," *Respirology*, vol. 15, no. 2, pp. 220–240, 2010.
- [12] W. Y. N. Naing and Z. Z. Htike, "Advances in automatic tuberculosis detection in chest x-ray images," *Signal & Image Processing*, vol. 5, no. 6, p. 41, 2014.
- [13] K. Nakamura, A. Ohmi, T. Kurihara, S. Suzuki, and M. Tadera, "Studies on the diagnostic value of 70 mm radiophotograms by mirror camera and the reading ability of physicians," *Kekkaku (Tuberculosis)*, vol. 45, no. 4, pp. 121–128, 1970.
- [14] N. M. Noor, O. M. Rijal, A. Yunus, A. A. Mahayiddin, G. C. Peng, and S. Abu-Bakar, "A statistical interpretation of the chest radiograph for the detection of pulmonary tuberculosis," in *2010 IEEE EMBS Conference on Biomedical Engineering and Sciences (IECBES)*. IEEE, 2010, pp. 47–51.
- [15] D. L. Cohn, R. J. OBrien, L. J. Geiter, F. Gordin, E. Hershfield, C. Horsburgh *et al.*, "Targeted tuberculin testing and treatment of latent tuberculosis infection," *MMWR Morb Mortal Wkly Rep*, vol. 49, no. 6, pp. 1–54, 2000.
- [16] A. Zwerling, S. van den Hof, J. Scholten, F. Cobelens, D. Menzies, and M. Pai, "Interferon-gamma release assays for tuberculosis screening of healthcare workers: A systematic review," *Thorax*, vol. 67, no. 1, pp. 62–70, 2012.
- [17] A. Lalvani and M. Pareek, "Interferon gamma release assays: Principles and practice," *Enfermedades Infecciosas Y Microbiologia Clinica*, vol. 28, no. 4, pp. 245–252, 2010.
- [18] P. Desikan, "Sputum smear microscopy in tuberculosis: Is it still relevant?" *The Indian Journal of Medical Research*, vol. 137, no. 3, p. 442, 2013.
- [19] P. C. Hopewell, M. Pai, D. Maher, M. Uplekar, and M. C. Raviglione, "International standards for tuberculosis care," *The Lancet Infectious Diseases*, vol. 6, no. 11, pp. 710–725, 2006.
- [20] G. Theron, R. Venter, G. Calligaro, L. Smith, J. Limberis, R. Meldau, D. Chanda, A. Esmail, J. Peter, and K. Dheda, "Xpert mtb/rif results in patients with previous tuberculosis: Can we distinguish true from false positive results?" *Clinical Infectious Diseases*, vol. 62, no. 8, pp. 995–1001, 2016.
- [21] J. Palomino, H. Traore, K. Fissette, and F. Portaels, "Evaluation of mycobacteria growth indicator tube (mgit) for drug susceptibility testing of mycobacterium tuberculosis," *The International Journal of Tuberculosis and Lung Disease*, vol. 3, no. 4, pp. 344–348, 1999.
- [22] E. Macondo, F. Ba, A. Gaye-Diallo, N. Touré-Kane, O. Kar` ré, A. Gueye-Ndiaye, C. Boye, and S. Mboup, "Rapid susceptibility testing of mycobacterium tuberculosis by the mycobacteria growth indicator tube (mgit ast sire)," *Clinical Microbiology and Infection*, vol. 6, no. 7, pp. 361–365, 2000.
- [23] M. Palaci, S. Ueki, D. N. Sato, M. D. S. Telles, M. Curcio, and E. Silva, "Evaluation of mycobacteria growth indicator tube for recovery and drug susceptibility testing of mycobacterium tuberculosis isolates from respiratory specimens," *Journal of Clinical Microbiology*, vol. 34, no. 3, pp. 762–764, 1996.
- [24] D. I. Ling, A. A. Zwerling, and M. Pai, "Genotype mtbdr assays for the diagnosis of multidrug-resistant tuberculosis: A meta-analysis," *European Respiratory Journal*, vol. 32, no. 5, pp. 1165–1174, 2008.
- [25] D. G. Storla, S. Yimer, and G. A. Bjune, "A systematic review of delay in the diagnosis and treatment of tuberculosis," *BMC Public Health*, vol. 8, no. 1, p. 15, 2008.
- [26] W. H. Organization *et al.*, *Tuberculosis Prevalence Surveys: A Handbook*. World Health Organization, 2011.
- [27] J. Burrill, C. J. Williams, G. Bain, G. Conder, A. L. Hine, and R. R. Misra, "Tuberculosis: A radiologic review," *Radiographics*, vol. 27, no. 5, pp. 1255–1273, 2007.
- [28] A. F. Gelb, C. Leffler, A. Brewin, V. Mascatello, and H. A. Lyons, "Miliary tuberculosis," *American Review of Respiratory Disease*, vol. 108, no. 6, pp. 1327–1333, 1973.
- [29] A. C. Nachiappan, K. Rahbar, X. Shi, E. S. Guy, E. J. Mortani Barbosa Jr, G. S. Shroff, D. Ocazionez, A. E. Schlesinger, S. I. Katz, and M. M. Hammer, "Pulmonary tuberculosis: Role of radiology in diagnosis and management," *Radiographics*, vol. 37, no. 1, pp. 52–72, 2017.
- [30] J. H. Woodring, H. Vandiviere, A. Fried, M. Dillon, T. Williams, and I. Melvin, "Update: The radiographic features of pulmonary tuberculosis," *American Journal of Roentgenology*, vol. 146, no. 3, pp. 497–506, 1986.
- [31] H. P. McAdams, J. Erasmus, and J. A. Winter, "Radiologic manifestations of pulmonary tuberculosis," *Radiologic Clinics of North America*, vol. 33, no. 4, pp. 655–678, 1995.
- [32] E. Castañer, X. Gallardo, J. M. Mata, and L. Esteba, "Radiologic approach to the diagnosis of infectious pulmonary diseases in patients infected with the human immunodeficiency virus," *European Journal of Radiology*, vol. 51, no. 2, pp. 114–129, 2004.
- [33] S. D. Greenberg, D. Frager, B. Suster, S. Walker, C. Stavropoulos, and A. Rothpearl, "Active pulmonary tuberculosis in patients with aids: Spectrum of radiographic findings (including a normal appearance)," *Radiology*, vol. 193, no. 1, pp. 115–119, 1994.
- [34] A. Krizhevsky, I. Sutskever, and G. E. Hinton, "Imagenet classification with deep convolutional neural networks," in *Advances in Neural Information Processing Systems*, 2012, pp. 1097–1105.
- [35] K. Simonyan and A. Zisserman, "Very deep convolutional networks for large-scale image recognition," *ArXiv Preprint ArXiv:1409.1556*, 2014.
- [36] U. Lopes and J. F. Valiati, "Pre-trained convolutional neural networks as feature extractors for tuberculosis detection," *Computers in Biology and Medicine*, vol. 89, pp. 135–143, 2017.
- [37] R. Hooda, S. Sofat, S. Kaur, A. Mittal, and F. Meriaudeau, "Deep-learning: A potential method for tuberculosis detection using chest radiography," in *2017 IEEE International Conference on Signal and Image Processing Applications (ICSIPA)*. IEEE, 2017, pp. 497–502.
- [38] A. Rohilla, R. Hooda, and A. Mittal, "Tb detection in chest radiograph using deep learning architecture," *ICETETSM-17*, pp. 136–147, 2017.
- [39] C. Szegedy, W. Liu, Y. Jia, P. Sermanet, S. Reed, D. Anguelov, D. Erhan, V. Vanhoucke, and A. Rabinovich, "Going deeper with convolutions," in *Proceedings of the IEEE Conference on Computer Vision and Pattern Recognition*, 2015, pp. 1–9.
- [40] P. Lakhani and B. Sundaram, "Deep learning at chest radiography: Automated classification of pulmonary tuberculosis by using convolutional neural networks," *Radiology*, vol. 284, no. 2, pp. 574–582, 2017.

- [41] C. Liu, Y. Cao, M. Alcantara, B. Liu, M. Brunette, J. Peinado, and W. Curioso, "Tx-cnn: Detecting tuberculosis in chest x-ray images using convolutional neural network," in *2017 IEEE International Conference on Image Processing (ICIP)*. IEEE, 2017, pp. 2314–2318.
- [42] K. He, X. Zhang, S. Ren, and J. Sun, "Deep residual learning for image recognition," in *Proceedings of the IEEE Conference on Computer Vision and Pattern Recognition*, 2016, pp. 770–778.
- [43] M. Abdi and S. Nahavandi, "Multi-residual networks: Improving the speed and accuracy of residual networks," *ArXiv Preprint ArXiv:1609.05672*, 2016.
- [44] X. Zhang, Z. Li, C. Change Loy, and D. Lin, "Polynet: A pursuit of structural diversity in very deep networks," in *Proceedings of the IEEE Conference on Computer Vision and Pattern Recognition*, 2017, pp. 718–726.
- [45] A. Veit, M. J. Wilber, and S. Belongie, "Residual networks behave like ensembles of relatively shallow networks," in *Advances in Neural Information Processing Systems*, 2016, pp. 550–558.
- [46] F. N. Iandola, S. Han, M. W. Moskewicz, K. Ashraf, W. J. Dally, and K. Keutzer, "Squeezenet: Alexnet-level accuracy with 50x fewer parameters and 0.5 mb model size," *ArXiv Preprint ArXiv:1602.07360*, 2016.
- [47] F. Mamalet and C. Garcia, "Simplifying convnets for fast learning," in *International Conference on Artificial Neural Networks*. Springer, 2012, pp. 58–65.
- [48] F. Chollet, "Xception: Deep learning with depthwise separable convolutions," in *Proceedings of the IEEE Conference on Computer Vision and Pattern Recognition*, 2017, pp. 1251–1258.
- [49] S. Sabour, N. Frosst, and G. E. Hinton, "Dynamic routing between capsules," in *Advances in Neural Information Processing Systems*, 2017, pp. 3856–3866.
- [50] T. Karnkawinpong and Y. Limpiyakorn, "Chest x-ray analysis of tuberculosis by convolutional neural networks with affine transforms," in *Proceedings of the 2018 2nd International Conference on Computer Science and Artificial Intelligence*, 2018, pp. 90–93.
- [51] M. D. Zeiler and R. Fergus, "Visualizing and understanding convolutional networks," in *European Conference on Computer Vision*. Springer, 2014, pp. 818–833.
- [52] G. Larsson, M. Maire, and G. Shakhnarovich, "Fractalnet: Ultra-deep neural networks without residuals," *ArXiv Preprint ArXiv:1605.07648*, 2016.
- [53] G. Huang, Z. Liu, L. Van Der Maaten, and K. Q. Weinberger, "Densely connected convolutional networks," in *Proceedings of the IEEE Conference on Computer Vision and Pattern Recognition*, 2017, pp. 4700–4708.
- [54] M. Lin, Q. Chen, and S. Yan, "Network in network," *ArXiv Preprint ArXiv:1312.4400*, 2013.
- [55] S. Ren, K. He, R. Girshick, and J. Sun, "Faster r-cnn: Towards real-time object detection with region proposal networks," in *Advances in Neural Information Processing Systems*, 2015, pp. 91–99.
- [56] S. Hwang, H.-E. Kim, J. Jeong, and H.-J. Kim, "A novel approach for tuberculosis screening based on deep convolutional neural networks," in *Medical Imaging 2016: Computer-Aided Diagnosis*, vol. 9785. International Society for Optics and Photonics, 2016, p. 97852W.
- [57] F. Pasa, V. Golkov, F. Pfeiffer, D. Cremers, and D. Pfeiffer, "Efficient deep network architectures for fast chest x-ray tuberculosis screening and visualization," *Scientific Reports*, vol. 9, no. 1, pp. 1–9, 2019.
- [58] S. Candemir, S. Jaeger, K. Palaniappan, J. P. Musco, R. K. Singh, Z. Xue, A. Karargyris, S. Antani, G. Thoma, and C. J. McDonald, "Lung segmentation in chest radiographs using anatomical atlases with nonrigid registration," *IEEE Transactions on Medical Imaging*, vol. 33, no. 2, pp. 577–590, 2013.
- [59] J. Irvin, P. Rajpurkar, M. Ko, Y. Yu, S. Ciurea-Ilcus, C. Chute, H. Marklund, B. Haghighi, R. Ball, K. Shpanskaya *et al.*, "Chexpert: A large chest radiograph dataset with uncertainty labels and expert comparison," in *Proceedings of the AAAI Conference on Artificial Intelligence*, vol. 33, 2019, pp. 590–597.
- [60] A. E. Johnson, T. J. Pollard, S. Berkowitz, N. R. Greenbaum, M. P. Lungren, C.-y. Deng, R. G. Mark, and S. Horng, "Mimic-cxr: A large publicly available database of labeled chest radiographs," *ArXiv Preprint ArXiv:1901.07042*, vol. 1, no. 2, 2019.
- [61] X. Wang, Y. Peng, L. Lu, Z. Lu, M. Bagheri, and R. M. Summers, "Chestx-ray8: Hospital-scale chest x-ray database and benchmarks on weakly-supervised classification and localization of common thorax diseases," in *Proceedings of the IEEE Conference on Computer Vision and Pattern Recognition*, 2017, pp. 2097–2106.
- [62] K. Murphy, S. S. Habib, S. M. A. Zaidi, S. Khowaja, A. Khan, J. Melendez, E. T. Scholten, F. Amad, S. Schalekamp, M. Verhagen *et al.*, "Computer aided detection of tuberculosis on chest radiographs: An evaluation of the cad4tb v6 system," *Scientific Reports*, vol. 10, no. 1, pp. 1–11, 2020.
- [63] T. Xu, I. Cheng, R. Long, and M. Mandal, "Novel coarse-to-fine dual scale technique for tuberculosis cavity detection in chest radiographs," *EURASIP Journal on Image and Video Processing*, vol. 2013, no. 1, p. 3, 2013.
- [64] E. J. Hwang, S. Park, K.-N. Jin, J. I. Kim, S. Y. Choi, J. H. Lee, J. M. Goo, J. Aum, J.-J. Yim, C. M. Park *et al.*, "Development and validation of a deep learning-based automatic detection algorithm for active pulmonary tuberculosis on chest radiographs," *Clinical Infectious Diseases*, vol. 69, no. 5, pp. 739–747, 2019.
- [65] W. H. Organization *et al.*, "Who report 2011: Global tuberculosis control. geneva: Who," *HTM/TB/2011.16*, Tech. Rep., 2011.
- [66] W. H. Organization and Others, "World health organization multidrug and extensively drug-resistant tb (m/xdr-tb): 2010 global report on surveillance and response. world health organization, geneva, switzerland," 2010.
- [67] K. Weyer, S. Carai, and P. Nunn, "Viewpoint tb diagnostics: What does the world really need?" *Journal of Infectious Diseases*, vol. 204, no. suppl\_4, pp. S1196–S1202, 2011.
- [68] E. Keeler, M. D. Perkins, P. Small, C. Hanson, S. Reed, J. Cunningham, J. E. Aledort, L. Hillborne, M. E. Rafael, F. Girosi *et al.*, "Reducing the global burden of tuberculosis: The contribution of improved diagnostics," *Nature*, vol. 444, no. 1, pp. 49–57, 2006.
- [69] D. L. Olson and D. Delen, *Advanced Data Mining Techniques*. Springer Science & Business Media, 2008.
- [70] M. T. Islam, M. A. Aowal, A. T. Minhaz, and K. Ashraf, "Abnormality detection and localization in chest x-rays using deep convolutional neural networks," *ArXiv Preprint ArXiv:1705.09850*, 2017.
- [71] A. G. Lalkhen and A. McCluskey, "Clinical tests: Sensitivity and specificity," *Continuing Education in Anaesthesia Critical Care & Pain*, vol. 8, no. 6, pp. 221–223, 2008.
- [72] D. G. Altman and J. M. Bland, "Diagnostic tests. 1: Sensitivity and specificity," *BMJ: British Medical Journal*, vol. 308, no. 6943, p. 1552, 1994.
- [73] S. A. Alasadi and W. S. Bhaya, "Review of data preprocessing techniques in data mining," *Journal of Engineering and Applied Sciences*, vol. 12, no. 16, pp. 4102–4107, 2017.
- [74] M. Sonka, V. Hlavac, and R. Boyle, *Image Processing, Analysis, and Machine Vision*. Cengage Learning, 2014.
- [75] S. García, J. Luengo, and F. Herrera, *Data Preprocessing in Data Mining*. Springer, 2015, vol. 72.
- [76] C. Qin, D. Yao, Y. Shi, and Z. Song, "Computer-aided detection in chest radiography based on artificial intelligence: A survey," *Biomedical Engineering Online*, vol. 17, no. 1, p. 113, 2018.
- [77] L. Xiao, C. Li, Z. Wu, and T. Wang, "An enhancement method for x-ray image via fuzzy noise removal and homomorphic filtering," *Neurocomputing*, vol. 195, pp. 56–64, 2016.
- [78] A. G. Webb, *Introduction to Biomedical Imaging*. John Wiley & Sons, 2017.
- [79] B. Kwan and H. K. Kwan, "Improved lung nodule visualization on chest radiographs using digital filtering and contrast enhancement," *World Acad Sci Eng Technol*, vol. 110, pp. 590–3, 2011.
- [80] A. Singh, S. Yadav, and N. Singh, "Contrast enhancement and brightness preservation using global-local image enhancement techniques," in *2016 Fourth International Conference On Parallel, Distributed and Grid Computing (Pdgc)*. IEEE, 2016, pp. 291–294.
- [81] L. Wang, J. Lu, Y. Li, T. Yahagi, and T. Okamoto, "Noise removal for medical x-ray images in wavelet domain," *Electrical Engineering in Japan*, vol. 163, no. 3, pp. 37–46, 2008.
- [82] C. Behrenbruch, S. Petroudi, S. Bond, J. Declerck, F. Leong, and J. Brady, "Image filtering techniques for medical image post-processing: An overview," *The British Journal of Radiology*, vol. 77, no. suppl\_2, pp. S126–S132, 2004.
- [83] X. Li, S. Luo, Q. Hu, J. Li, and D. Wang, "Rib suppression in chest radiographs for lung nodule enhancement," in *2015 IEEE International Conference on Information and Automation*. IEEE, 2015, pp. 50–55.
- [84] K. Suzuki, H. Abe, H. MacMahon, and K. Doi, "Image-processing technique for suppressing ribs in chest radiographs by means of massive training artificial neural network (mtann)," *IEEE Transactions on Medical Imaging*, vol. 25, no. 4, pp. 406–416, 2006.
- [85] M. Loog and B. van Ginneken, "Bony structure suppression in chest radiographs," in *International Workshop on Computer Vision Approaches to Medical Image Analysis*. Springer, 2006, pp. 166–177.
- [86] P. Maduskar, L. Hogeweg, R. Philipsen, S. Schalekamp, and B. Van Ginneken, "Improved texture analysis for automatic detection of tuberculosis (tb) on chest radiographs with bone suppression images," in *Medical Imaging 2013: Computer-Aided Diagnosis*, vol. 8670. International Society for Optics and Photonics, 2013, p. 86700H.

- [87] F. Li, R. Engelmann, L. Pesce, S. G. Armato, and H. MacMahon, "Improved detection of focal pneumonia by chest radiography with bone suppression imaging," *European Radiology*, vol. 22, no. 12, pp. 2729–2735, 2012.
- [88] Y. Gordienko, P. Gang, J. Hui, W. Zeng, Y. Kochura, O. Alienin, O. Rokovy, and S. Stirenko, "Deep learning with lung segmentation and bone shadow exclusion techniques for chest x-ray analysis of lung cancer," in *International Conference on Computer Science, Engineering and Education Applications*. Springer, 2018, pp. 638–647.
- [89] H. X. Nguyen and T. T. Dang, "Ribs suppression in chest x-ray images by using ica method," in *5th International Conference on Biomedical Engineering in Vietnam*. Springer, 2015, pp. 194–197.
- [90] W. Yang, Y. Chen, Y. Liu, L. Zhong, G. Qin, Z. Lu, Q. Feng, and W. Chen, "Cascade of multi-scale convolutional neural networks for bone suppression of chest radiographs in gradient domain," *Medical Image Analysis*, vol. 35, pp. 421–433, 2017.
- [91] J. von Berg, C. Levrier, H. Carolus, S. Young, A. Saalbach, P. Laurent, and R. Florent, "Decomposing the bony thorax in x-ray images," in *2016 IEEE 13th International Symposium on Biomedical Imaging (ISBI)*. IEEE, 2016, pp. 1068–1071.
- [92] B. Van Ginneken, B. T. H. Romeny, and M. A. Viergever, "Computer-aided diagnosis in chest radiography: A survey," *IEEE Transactions on Medical Imaging*, vol. 20, no. 12, pp. 1228–1241, 2001.
- [93] S. G. Armato III, M. L. Giger, and H. MacMahon, "Automated lung segmentation in digitized posteroanterior chest radiographs," *Academic Radiology*, vol. 5, no. 4, pp. 245–255, 1998.
- [94] L. Li, Y. Zheng, M. Kallergi, and R. A. Clark, "Improved method for automatic identification of lung regions on chest radiographs," *Academic Radiology*, vol. 8, no. 7, pp. 629–638, 2001.
- [95] D. Cheng and M. Goldberg, "An algorithm for segmenting chest radiographs," in *Visual Communications and Image Processing '88: Third in a Series*, vol. 1001. International Society for Optics and Photonics, 1988, pp. 261–268.
- [96] D. K. Iakovidis and G. Papamichalis, "Automatic segmentation of the lung fields in portable chest radiographs based on bézier interpolation of salient control points," in *2008 IEEE International Workshop on Imaging Systems and Techniques*. IEEE, 2008, pp. 82–87.
- [97] B. Van Ginneken and B. M. ter Haar Romeny, "Automatic segmentation of lung fields in chest radiographs," *Medical Physics*, vol. 27, no. 10, pp. 2445–2455, 2000.
- [98] A. Mittal, R. Hooda, and S. Sofat, "Lung field segmentation in chest radiographs: A historical review, current status, and expectations from deep learning," *IET Image Processing*, vol. 11, no. 11, pp. 937–952, 2017.
- [99] N. F. Vittitoe, R. Vargas-Voracek, and C. E. Floyd Jr, "Markov random field modeling in posteroanterior chest radiograph segmentation," *Medical Physics*, vol. 26, no. 8, pp. 1670–1677, 1999.
- [100] Z. Yue, A. Goshtasby, and L. V. Ackerman, "Automatic detection of rib borders in chest radiographs," *IEEE Transactions on Medical Imaging*, vol. 14, no. 3, pp. 525–536, 1995.
- [101] B. Van Ginneken, M. B. Stegmann, and M. Loog, "Segmentation of anatomical structures in chest radiographs using supervised methods: A comparative study on a public database," *Medical Image Analysis*, vol. 10, no. 1, pp. 19–40, 2006.
- [102] T. McInerney and D. Terzopoulos, "Deformable models in medical image analysis: A survey," *Medical Image Analysis*, vol. 1, no. 2, pp. 91–108, 1996.
- [103] B. Van Ginneken, S. Katsuragawa, B. M. ter Haar Romeny, K. Doi, and M. A. Viergever, "Automatic detection of abnormalities in chest radiographs using local texture analysis," *IEEE Transactions on Medical Imaging*, vol. 21, no. 2, pp. 139–149, 2002.
- [104] I. Matthews and S. Baker, "Active appearance models revisited," *International Journal of Computer Vision*, vol. 60, no. 2, pp. 135–164, 2004.
- [105] T. F. Cootes, G. J. Edwards, and C. J. Taylor, "Active appearance models," *IEEE Transactions on Pattern Analysis and Machine Intelligence*, vol. 23, no. 6, pp. 681–685, 2001.
- [106] T. F. Cootes, C. J. Taylor, D. H. Cooper, and J. Graham, "Active shape models—their training and application," *Computer Vision and Image Understanding*, vol. 61, no. 1, pp. 38–59, 1995.
- [107] N. N. K. Chi, "Active shape models their training and application," Ph.D. dissertation, International University HCMC, Vietnam, 2011.
- [108] A. Dawoud, "Lung segmentation in chest radiographs by fusing shape information in iterative thresholding," *IET Computer Vision*, vol. 5, no. 3, pp. 185–190, 2011.
- [109] N. Babaii Rizvandi, A. Pizurica, and W. Philips, "Active appearance model (aam)-from theory to implementation," in *3rd International Conference on Computer Vision Theory and Applications*. INSTICC, 2008, pp. 539–542.
- [110] Y. Shi, F. Qi, Z. Xue, L. Chen, K. Ito, H. Matsuo, and D. Shen, "Segmenting lung fields in serial chest radiographs using both population-based and patient-specific shape statistics," *IEEE Transactions on Medical Imaging*, vol. 27, no. 4, pp. 481–494, 2008.
- [111] B. Van Ginneken, A. F. Frangi, J. J. Staal, B. M. ter Haar Romeny, and M. A. Viergever, "Active shape model segmentation with optimal features," *IEEE Transactions on Medical Imaging*, vol. 21, no. 8, pp. 924–933, 2002.
- [112] P. Annangi, S. Thiruvankadam, A. Raja, H. Xu, X. Sun, and L. Mao, "A region based active contour method for x-ray lung segmentation using prior shape and low level features," in *2010 IEEE International Symposium on Biomedical Imaging: From Nano to Macro*. IEEE, 2010, pp. 892–895.
- [113] S. Jaeger, A. Karargyris, S. Antani, and G. Thoma, "Detecting tuberculosis in radiographs using combined lung masks," in *2012 Annual International Conference of the IEEE Engineering in Medicine and Biology Society*. IEEE, 2012, pp. 4978–4981.
- [114] W. S. H. M. W. Ahmad, W. M. D. W. Zaki, and M. F. A. Fauzi, "Lung segmentation on standard and mobile chest radiographs using oriented gaussian derivatives filter," *Biomedical Engineering Online*, vol. 14, no. 1, p. 20, 2015.
- [115] N. Y. Ilyasova, A. Shirokanev, and N. Demin, "Segmentation of lung images using textural features," in *Journal of Physics: Conference Series*, vol. 1438. IOP Publishing, 2020, p. 012015.
- [116] Z. Shi, P. Zhou, L. He, T. Nakamura, Q. Yao, and H. Itoh, "Lung segmentation in chest radiographs by means of gaussian kernel-based fcm with spatial constraints," in *2009 Sixth International Conference on Fuzzy Systems and Knowledge Discovery*, vol. 3. IEEE, 2009, pp. 428–432.
- [117] N. F. Vittitoe, R. Vargas-Voracek, and C. E. Floyd Jr, "Identification of lung regions in chest radiographs using markov random field modeling," *Medical Physics*, vol. 25, no. 6, pp. 976–985, 1998.
- [118] S. Candemir, S. Jaeger, K. Palaniappan, S. Antani, and G. Thoma, "Graph-cut based automatic lung boundary detection in chest radiographs," in *IEEE Healthcare Technology Conference: Translational Engineering in Health & Medicine*, 2012, pp. 31–34.
- [119] M. F. McNitt-Gray, J. W. Sayre, H. Huang, and M. Razavi, "Pattern classification approach to segmentation of chest radiographs," in *Medical Imaging 1993: Image Processing*, vol. 1898. International Society for Optics and Photonics, 1993, pp. 160–170.
- [120] H. Ng, S. Ong, K. Foong, P. Goh, and W. Nowinski, "Medical image segmentation using k-means clustering and improved watershed algorithm," in *2006 IEEE Southwest Symposium on Image Analysis and Interpretation*. IEEE, 2006, pp. 61–65.
- [121] C. H. Bindu and K. S. Prasad, "An efficient medical image segmentation using conventional otsu method," *International Journal of Advanced Science and Technology*, vol. 38, no. 1, pp. 67–74, 2012.
- [122] R. Girshick, J. Donahue, T. Darrell, and J. Malik, "Region-based convolutional networks for accurate object detection and segmentation," *IEEE Transactions on Pattern Analysis and Machine Intelligence*, vol. 38, no. 1, pp. 142–158, 2015.
- [123] C. Gu, J. J. Lim, P. Arbeláez, and J. Malik, "Recognition using regions," in *2009 IEEE Conference on Computer Vision and Pattern Recognition*. IEEE, 2009, pp. 1030–1037.
- [124] A. A. Novikov, D. Lenis, D. Major, J. Hladuvka, M. Wimmer, and K. Bühler, "Fully convolutional architectures for multiclass segmentation in chest radiographs," *IEEE Transactions on Medical Imaging*, vol. 37, no. 8, pp. 1865–1876, 2018.
- [125] J. Long, E. Shelhamer, and T. Darrell, "Fully convolutional networks for semantic segmentation," in *Proceedings of the IEEE Conference on Computer Vision and Pattern Recognition*, 2015, pp. 3431–3440.
- [126] M. Günel, "Googlenet," 2016.
- [127] H. Jun, L. Shuai, S. Jinming, L. Yue, W. Jingwei, and J. Peng, "Facial expression recognition based on vggnet convolutional neural network," in *2018 Chinese Automation Congress (CAC)*. IEEE, 2018, pp. 4146–4151.
- [128] F. Ning, D. Delhomme, Y. LeCun, F. Piano, L. Bottou, and P. E. Barbano, "Toward automatic phenotyping of developing embryos from videos," *IEEE Transactions on Image Processing*, vol. 14, no. 9, pp. 1360–1371, 2005.
- [129] W. Dai, N. Dong, Z. Wang, X. Liang, H. Zhang, and E. P. Xing, "Scan: Structure correcting adversarial network for organ segmentation in chest x-rays," in *Deep Learning in Medical Image Analysis and Multimodal Learning for Clinical Decision Support*. Springer, 2018, pp. 263–273.
- [130] J. Hofmanninger, F. Prayer, J. Pan, S. Rohrich, H. Prosch, and G. Langs, "Automatic lung segmentation in routine imaging is a data diversity problem, not a methodology problem," *ArXiv Preprint ArXiv:2001.11767*, 2020.

- [131] Y. Zhang, S. Miao, T. Mansi, and R. Liao, "Unsupervised x-ray image segmentation with task driven generative adversarial networks," *Medical Image Analysis*, vol. 62, p. 101664, 2020.
- [132] M. Kholiavchenko, I. Sirazitdinov, K. Kubrak, R. Badrutdinova, R. Kuleev, Y. Yuan, T. Vrtovec, and B. Ibragimov, "Contour-aware multi-label chest x-ray organ segmentation," *International Journal of Computer Assisted Radiology and Surgery*, vol. 15, no. 3, pp. 425–436, 2020.
- [133] M. Oloko-Oba and S. Viriri, "Diagnosing tuberculosis using deep convolutional neural network," in *International Conference on Image and Signal Processing*. Springer, 2020, pp. 151–161.
- [134] K. Munadi, K. Muchtar, N. Maulina, and B. Pradhan, "Image enhancement for tuberculosis detection using deep learning," *IEEE Access*, vol. 8, pp. 217 897–217 907, 2020.
- [135] N. M. Noor, O. Rijal, and Y. Fah, "Wavelet as features for tuberculosis (mtb) using standard x-ray film images," in *6th International Conference on Signal Processing, 2002.*, vol. 2. IEEE, 2002, pp. 1138–1141.
- [136] T. Rahman, A. Khandakar, M. A. Kadir, K. R. Islam, K. F. Islam, R. Mazhar, T. Hamid, M. T. Islam, S. Kashem, Z. B. Mahbub *et al.*, "Reliable tuberculosis detection using chest x-ray with deep learning, segmentation and visualization," *IEEE Access*, vol. 8, pp. 191 586–191 601, 2020.
- [137] B. Antony and N. B. PK, "Lung tuberculosis detection using x-ray images," *International Journal of Applied Engineering Research*, vol. 12, no. 24, pp. 15 196–15 201, 2017.
- [138] I. Gabriella *et al.*, "Early detection of tuberculosis using chest x-ray (cxr) with computer-aided diagnosis," in *2018 2nd International Conference on Biomedical Engineering (IBIOMED)*. IEEE, 2018, pp. 76–79.
- [139] R. Khutlang, S. Krishnan, R. Dendere, A. Whitelaw, K. Veropoulos, G. Learmonth, and T. S. Douglas, "Classification of mycobacterium tuberculosis images of zn-stained sputum smears," *IEEE Transactions on Information Technology in biomedicine*, vol. 14, no. 4, pp. 949–957, 2009.
- [140] R. N. Rohmah, A. Susanto, and I. Soesanti, "Lung tuberculosis identification based on statistical feature of thoracic x-ray," in *2013 International Conference on QIR*. IEEE, 2013, pp. 19–26.
- [141] M. Oloko-Oba and S. Viriri, "Tuberculosis abnormality detection in chest x-rays: A deep learning approach," in *International Conference on Computer Vision and Graphics*. Springer, 2020, pp. 121–132.
- [142] A. Koeslag and G. de Jager, "Computer aided diagnosis of miliary tuberculosis," *Proceedings of the Pattern Recognition Association of South Africa*, 2001.
- [143] Y.-L. Song and Y. Yang, "Localization algorithm and implementation for focal of pulmonary tuberculosis chest image," in *2010 International Conference on Machine Vision and Human-Machine Interface*. IEEE, 2010, pp. 361–364.
- [144] Y. Arzhaeva, L. Hogeweg, P. A. de Jong, M. A. Viergever, and B. van Ginneken, "Global and local multi-valued dissimilarity-based classification: Application to computer-aided detection of tuberculosis," in *International Conference on Medical Image Computing and Computer-Assisted Intervention*. Springer, 2009, pp. 724–731.
- [145] S. Hariharan, A. Ray, and M. Ghosh, "An algorithm for the enhancement of chest x-ray images of tuberculosis patients," in *Proceedings of IEEE International Conference on Industrial Technology 2000 (IEEE Cat. No. 00TH8482)*, vol. 2. IEEE, 2000, pp. 107–112.
- [146] A. Chauhan, D. Chauhan, and C. Rout, "Role of gist and phog features in computer-aided diagnosis of tuberculosis without segmentation," *PLoS One*, vol. 9, no. 11, 2014.
- [147] K. Le, "Automated detection of early lung cancer and tuberculosis based on x-ray image analysis," in *Proc. WSEAS International Conference on Signal, Speech and Image Processing*, 2006, pp. 1–6.
- [148] P. Rajpurkar, J. Irvin, R. L. Ball, K. Zhu, B. Yang, H. Mehta, T. Duan, D. Ding, A. Bagul, C. P. Langlotz *et al.*, "Deep learning for chest radiograph diagnosis: A retrospective comparison of the chexnext algorithm to practicing radiologists," *PLoS Medicine*, vol. 15, no. 11, p. e1002686, 2018.
- [149] Y. Bar, I. Diamant, L. Wolf, S. Lieberman, E. Konen, and H. Greenspan, "Chest pathology detection using deep learning with non-medical training," in *2015 IEEE 12th International Symposium on Biomedical Imaging (ISBI)*. IEEE, 2015, pp. 294–297.
- [150] R. Singh, M. K. Kalra, C. Nitiwarangkul, J. A. Patti, F. Homayounieh, A. Padole, P. Rao, P. Putha, V. V. Muse, A. Sharma *et al.*, "Deep learning in chest radiography: Detection of findings and presence of change," *PLoS One*, vol. 13, no. 10, 2018.
- [151] S.-J. Heo, Y. Kim, S. Yun, S.-S. Lim, J. Kim, C.-M. Nam, E.-C. Park, I. Jung, and J.-H. Yoon, "Deep learning algorithms with demographic information help to detect tuberculosis in chest radiographs in annual workers health examination data," *International Journal of Environmental Research and Public Health*, vol. 16, no. 2, p. 250, 2019.
- [152] R. D. J. Samuel and B. R. Kanna, "Tuberculosis (tb) detection system using deep neural networks," *Neural Computing and Applications*, vol. 31, no. 5, pp. 1533–1545, 2019.
- [153] M. Cicero, A. Bilbily, E. Colak, T. Dowdell, B. Gray, K. Perampaladas, and J. Barfett, "Training and validating a deep convolutional neural network for computer-aided detection and classification of abnormalities on frontal chest radiographs," *Investigative Radiology*, vol. 52, no. 5, pp. 281–287, 2017.
- [154] A. Hamadi, N. B. Cheikh, Y. Zouatine, S. M. B. Menad, and M. R. Djebbara, "Imageclef 2019: Deep learning for tuberculosis ct image analysis," *CLEF2019 Working Notes*, vol. 2380, pp. 9–12, 2019.
- [155] M. Oloko-Oba and S. Viriri, "Pre-trained convolutional neural network for the diagnosis of tuberculosis," in *International Symposium on Visual Computing*. Springer, 2020, pp. 558–569.
- [156] M. Nash, R. Kadavigere, J. Andrade, C. A. Sukumar, K. Chawla, V. P. Shenoy, T. Pande, S. Huddart, M. Pai, and K. Saravu, "Deep learning, computer-aided radiography reading for tuberculosis: A diagnostic accuracy study from a tertiary hospital in india," *Scientific Reports*, vol. 10, no. 1, pp. 1–10, 2020.
- [157] P. Putha, M. Tadepalli, B. Reddy, T. Raj, J. A. Chiramal, S. Govil, N. Sinha, M. KS, S. Reddivari, A. Jagirdar *et al.*, "Can artificial intelligence reliably report chest x-rays?: Radiologist validation of an algorithm trained on 2.3 million x-rays," *ArXiv Preprint ArXiv:1807.07455*, 2018.
- [158] Z. U. Abideen, M. Ghafoor, K. Munir, M. Saqib, A. Ullah, T. Zia, S. A. Tariq, G. Ahmed, and A. Zahra, "Uncertainty assisted robust tuberculosis identification with bayesian convolutional neural networks," *IEEE Access*, vol. 8, pp. 22 812–22 825, 2020.
- [159] M. Oloko-Oba and S. Viriri, "Ensemble of convolution neural networks for automatic tuberculosis classification," in *International Conference on Computational Collective Intelligence*. Springer, 2021, pp. 549–559.
- [160] S. Rajaraman and S. K. Antani, "Modality-specific deep learning model ensembles toward improving tb detection in chest radiographs," *IEEE Access*, vol. 8, pp. 27 318–27 326, 2020.
- [161] M. H. A. Hijazi, S. K. T. Hwa, A. Bade, R. Yaakob, and M. S. Jeffree, "Ensemble deep learning for tuberculosis detection using chest x-ray and canny edge detected images," *IAES International Journal of Artificial Intelligence*, vol. 8, no. 4, p. 429, 2019.
- [162] A. T. Sahlol, M. Abd Elaziz, A. Tariq Jamal, R. Damaševičius, and O. Farouk Hassan, "A novel method for detection of tuberculosis in chest radiographs using artificial ecosystem-based optimisation of deep neural network features," *Symmetry*, vol. 12, no. 7, p. 1146, 2020.
- [163] R.-I. Chang, Y.-H. Chiu, and J.-W. Lin, "Two-stage classification of tuberculosis culture diagnosis using convolutional neural network with transfer learning," *The Journal of Supercomputing*, pp. 1–16, 2020.
- [164] M. Ayaz, F. Shaukat, and G. Raja, "Ensemble learning based automatic detection of tuberculosis in chest x-ray images using hybrid feature descriptors," *Physical and Engineering Sciences in Medicine*, vol. 44, no. 1, pp. 183–194, 2021.
- [165] M. Oloko-Oba and S. Viriri, "Ensemble of efficientnets for the diagnosis of tuberculosis," *Computational Intelligence and Neuroscience*, vol. 2021, 2021.
- [166] J. H. Tan, U. R. Acharya, C. Tan, K. T. Abraham, and C. M. Lim, "Computer-assisted diagnosis of tuberculosis: a first order statistical approach to chest radiograph," *Journal of medical systems*, vol. 36, no. 5, pp. 2751–2759, 2012.
- [167] R. Shen, I. Cheng, and A. Basu, "A hybrid knowledge-guided detection technique for screening of infectious pulmonary tuberculosis from chest radiographs," *IEEE transactions on biomedical engineering*, vol. 57, no. 11, pp. 2646–2656, 2010.